Supersonic 'Oblique All Wing' Airfoil Design

by

Matthew Elliott Butler

BEng/Hons University of Manchester (1990)

SUBMITTED TO THE DEPARTMENT OF
AERONAUTICS AND ASTRONAUTICS
IN PARTIAL FULFILLMENT OF THE REQUIREMENTS
FOR THE DEGREE OF

Master of Science
at the
Massachusetts Institute of Technology

September 1993

Signature of Author _____

Department of Aeronautics and Astronautics
August 9, 1993

Certified by _____

Professor Mark Drela
Thesis Supervisor, Department of Aeronautics and Astronautics

Accepted by _____

Professor Harold Y. Wachman
Chairman, Department Graduate Committee

Supersonic 'Oblique All Wing' Airfoil Design

by

Matthew Elliott Butler

Submitted to the Department of Aeronautics and Astronautics

on August 9, 1993

in partial fulfillment of the requirements for the degree of

Master of Science in Aeronautics and Astronautics

Inviscid analytical solutions, given by Jones and Smith for the wave drag due to lift, induced drag and wave drag due to volume of a skewed elliptic wing were combined with Drela's, viscous, 2D airfoil design code, MSES, which computes the profile drag (pressure drag and skin friction drag) in order to calculate the total drag of an "Oblique All Wing" style aircraft. Drela's optimization driver, LINDOP, was used to converge upon an airfoil with the greatest range paramerter, $\mathcal{R} = \frac{M_\infty L}{D}$, given a number of geometric and aerodynamic constraints. At the typical operating condition $M_\infty = 1.6$, $C_{L_\perp} = 0.65$, Λ (sweep) $= 64°$, the best range parameter achieved was $\mathcal{R} = 20.7$.

Thesis Supervisor: Mark Drela,

Associate Professor of Aeronautics and Astronautics

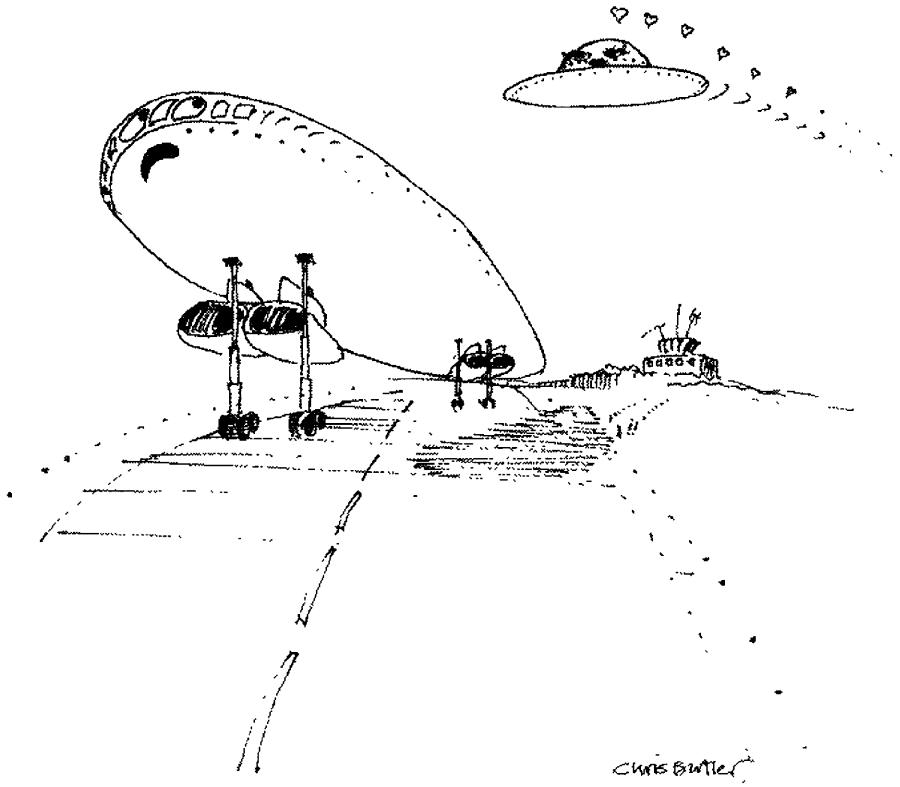
CHRIS BUTLER

Acknowledgments

Okay, first I must thank my parents and sister for putting up with years of stress and anxiety, broken bones and an MIT entrance application. You got me there, I'll take it from here.

Mark Drela. Thanks for your guaranteed office attendance during the final lap of my thesis as I inundated you with "quick" questions. You have inspired me and kept the sparkle of aviation alive with an unusual concoction of world records and beer poker – just keep letting me win at darts!

Scott Stephenson. Thanks mate for sharing this parallel Hell to completion. Your friendship and support was essential and much appreciated. I am especially grateful for your medicinal supply of laughter and your instigation of mental regression – keep taking the tablets.

Ted Liefeld. Thank you for preventing me from becoming an alcoholic by not letting me drink alone, for helping me paint the ski slopes red and the 'Poor House' green. Here's to Chamonix next year.

Pax (Rick Paxson). I am greatly in debt to you for your generosity and enthusiasm that one could build a plane with. I particularly enjoyed those coffee/vegetable-chilly problem solving sessions and look forward to future ones.

Marc Schafer. Thank you Marc for taking over, with the fun things in life, where I left off.

Michelle Butler. Patient, understanding and a total babe.

Finally, I would like to thank The Rght. Hon. Sir. Kenneth Baker and Kathy Hubbard for pulling the strings to allow my funding.

Contents

List of Figures

Chapter 1
Foreword

The aims of the study, though inherently related, were two-fold:

1. exemplify the power of the interactive optimization method, LINDOP[1] .
2. design the optimum airfoil section of an 'Oblique-All-Wing' (**OAW**) style supersonic aircraft of elliptic planform subject to "user-defined" constraints.

This report describes the method used to generate the airfoil shape so designed as to achieve the maximum range parameter, $\mathcal{R} = \frac{M_\infty L}{D}$ (see sections 4 & 4.1) , subject to user-defined constraints. Possible constraints include:

- the geometric span (runway width limitation),
- Cruise Mach number (airline influenced trade-off between travel time efficiency and fuel efficiency),
- airfoil geometry (structural/volume-occupancy limitation to satisfy torsion box cabin design) and
- altitude restrictions (government enforced control of chemical pollution to the environment).

This work is primarily concerned with constraints on strategically positioned thicknesses over a selection of flight Mach numbers at fixed values of perpendicular lift coefficient (see figure 7.7 and equation 7.30).

Chapter 2
Report Layout

A loose summary of the report is stated in the abstract. Sections 3.1 and 3.2 give some history of oblique wing design concepts, point out areas of current activity and driving forces behind these types of supersonic transport (SST) interests. Chapter 4 and section 4.1 state the design objective of this report and introduce the single-point objective function that the optimization procedure is based upon. Chapter 5 sets out the physical situation and explains the model subdivisions. The limitations of the physical models are also stated. Chapter 6 describes the design method procedure, introduces a more robust objective function to optimize and gives an example of such. It also refers the reader forward for the exact methods by which the drag and lift were predicted and for the detailing of the optimization procedure. Chapter 7 details the drag predictions and their associated components of the objective function. A briefing of the optimization procedure is given in Chapter 8 and section 8.1 describes the involvement of subroutines written specifically to solve the problem posed by the title of this report. Chapter 9 lists, mathematically, the functional relationships of the individual components that make up the single point objective function and derives sensitivities required by the optimization procedure. Results of the example optimization set-up are described in Chapter 10 and conclusions of the overall report given in Chapter 11. Future improvements are discussed in Chapter 12. The three appendices list the nomenclature and the two optimization procedure routines fundamental to this report's analysis.

Chapter 3

Introduction

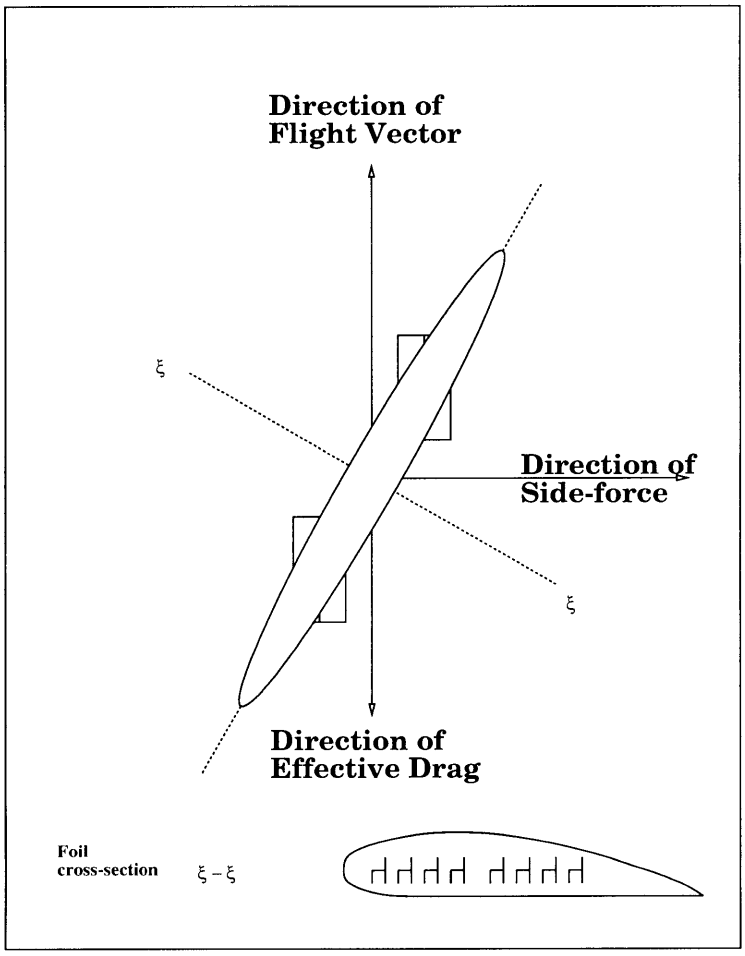

Figure 3.1: Oblique All Wing Concept.

3.1 Background on Oblique Wing Concepts

The minimum inviscid drag of a supersonic thin lifting surface is obtained when the induced downwash is constant over the planform. In 1951 Jones [2] showed that this can be achieved by distributing the lift elliptically both in the flight direction and the aerodynamic spanwise direction simultaneously. The simplest practical example seems to be that of the obliquely swept elliptic wing (figure 3.1). This report documents a method used to determine the correct sharing of lift between these orthogonal directions for given flight Mach numbers and user specifications. For a fixed planform this sharing can be controlled by variable sweep. Wave drag is reduced as the distribution of lift and thickness is elongated in the flight direction – which, for a given wing planform, implies increasing sweep. Increasing sweep, however, reduces the aerodynamic aspect ratio and so increases induced drag. Profile drag is that due to friction and pressure local to the airfoil. The friction is assumed to act straight backwards (ie. no account has be made for the spanwise perturbations of the skin friction forces) whilst the pressure drag originates in the perpendicular direction – so contributing to side-force as well as true drag.

Besides its minimum inviscid drag, the OAW offers other advantages. The basic geometry simplifies the manufacture and allows a higher than usual axis-ratio, σ [1], thus reducing both the induced and wave drag. The OAW is likely to fly with modest sweep angles at low speed and up to about 65° at a cruise Mach number of approximately 1.8. The OAW will thus naturally have a high aspect ratio on take-off. The resulting high $\frac{L}{D}$ available at take-off should ease some of the hurdles associated with take-off distance and noise regulations. With regards to the latter, the subsonic high lift characteristic of this craft may prove especially beneficial in dictating ground footprint noise patterns – so critical in dealing with "technopolitics". Relatively small amounts of sweep on take-off also reduces the necessity for cumbersome high lift devices that become a burden in supersonic flow (since $C_{Lmax} \sim \cos\Lambda^2$). The sonic booms observed at the earth's surface are due to the focusing of waves created by isentropic turning. Distributing the

[1] $\sigma = \frac{\tilde{b}}{\tilde{c}}$ (see figure 7.4) and is used where appropriate to avoid the ambiguity that Aspect-Ratio might create with the OAW configuration.

lift over a long axis eases the discomfort to ground observers.

NASA began flight-test work on transonic oblique wing concepts in 1973. They were primarily concerned with a single pivoting wing high mounted on a fuselage. A 20 ft. wingspan radio-controlled model was successfully built and flown. By 1978 they had the subsonic, jet-powered, AD-1 which flew 50 test flights until oil prices prevented further work. Later (1984), NASA commenced their program aimed at converting an F-8E Corsair to a single pivot oblique wing configuration with digital fly-by-wire technology. A great deal of promising wind tunnel results were achieved and CFD analysis undertaken but the project was dropped when the A-12 project, with its focus on stealthiness, began.

Commercial applications of the OAW have also been considered. Jones proposed a wing and body combination for an SST [3] to cruise at Mach 1.4 with the intention to reduce over-land sonic boom and take-off engine noise. Later, Boeing constructed a comparative study of transonic and low-supersonic transport aircraft. In the report of Jones and Nisbet [4] it was concluded that the oblique-wing airplane was better in terms of gross weight[2], fuel consumption and noise level but had less aeroelastic stability than a swept back configuration. Jones extended his studies of oblique wing aircraft design in 1976 [5], touching on aspects of flight control, trim, aeroelastic stability and the extension to flight at Mach 2.0.

Interest has fired up yet again. As a result of the trends in future planning – eg. reduction in Mach number estimates[6] and weighted importance of noise pollution – "NASA Ames Research Center has resumed its program to develop the technology for a supersonic, oblique wing aircraft after a pause of several years in the 30-year-old effort."[7] Aiming to carry 300-500 passengers between Mach 1.6 and 1.8., the aircraft would have a span of well over 100m, a chord of the order of 15m and a thickness of over 2m. The current proposal[8] suggests a take-off slew angle of 37.5° and an upper Mach limit of 1.8. The examples of airfoil design documented in this report are especially

[2]The (wing+fuselage) config. has structural benefits over its symmetric counterpart in that only one wing pivot is required and the loads borne are primarily tension and compression – leading to a reduction in necessary weight.

relevant to this current interest.

3.2 Commercial Viability

The technological potential to build an HSCT certainly exists. The hard part will be making it commercially viable [9, 10, 11]. According to some U.S. market studies there are clearly demands for such a vehicle[12, 13]. KLM, Lufthansa, SIA, JAL, Air France and BA have all expressed desires for the introduction of an HSCT around 2010[14]. There are, of course, many hurdles to overcome. The idea of supersonic civil transport has become somewhat of a melodramatic issue. "No's" are expressed before proposals are even made and a psychological game of politics must now be played. Physical problems exist too. Overland boom signature, engine noise on take-off and the latency of required technological solutions. But commercial success is possibly the biggest hurdle of all. Since the airline manufacturer collects his return from sales to airline companies he must guarantee these sales by offering a product that is commercially more successful than his competitors. The choice of product is crucial - these type of sales are low volume and thus there exists very little space for product differentiation. The result can be a win-lose situation as opposed to a graded scale of success. The objective of the airline is to maximize profits over a prescribed period of time. The costs include aircraft price, maintenance, labour, fuel etc. It is usual that fuel costs are the limiting factor but it is important to note that the airline company is providing a service. The airline may be able to increase its sale of seat-miles by offering a speedy transportation (thus weighting the curves of figure 6.1 to favor the higher Mach numbers). The antithesis would be the loss in seat-miles due to passenger reservations about flying in an 'unconventional' aircraft. It is likely that, although there may be market desire, there is only room (commercially) for one or two types of HSCT - once again increasing the risk stakes of pursuing such a project. But with the risks of taking on this venture are those of shying away. Momentum is gathering for an HSCT[15, 16] and NASA engineers believe that "the time is now right for the oblique wing."[7]. BA are planning more supersonic charters from the U.S.[17]. Anglo-French links were renewed for "The Son of Concorde"[18, 19] and the technology matched by Boeing and McDonnell Douglas[20].

The consensus of opinion seems to be a collaborate effort on an international scale. With such a venture, it seems no single manufacturer is able to bear the risk alone. Pratt & Whitney and General Electric have announced their plan to team together and Boeing and McDonnell Douglas joined the SST group that includes BA, Aerospatiale and Deutsche Airbus[18].

As an aside, it is interesting to see the possibility of a more hasty entrance into the civil supersonic transport market via the Supersonic Business Jet (SSBJ). Interest in this field has also been stirring for a while now – several design proposals have been studied by Gulfstream Aerospace Corp.[21, 22, 23]. The SSBJ has several redeeming characteristics. For one, the market is not so cut-throat and there are less "big-names" competing for survival. Customers are often driven more by issues of aesthetics than by fuel economy. The corporate jet conveys a certain image and customers may be prepared to pay over-the-odds to get it. The desire for speed may be stronger – saving travel time can be paramount to international business which, incidentally, is booming! An (oblique-wing+fuselage) SSBJ could certainly pander to the growing market demand, providing a "flashy" image as well as exploiting the physical benefits of the single wing pivot (structural weight and aircraft ground storage space savings).

Chapter 4
Design Objective

Assuming that fuel costs are the limiting factor (ignoring the travel time savings), the design objective is an aircraft that minimizes fuel costs per seat-mile. Increasing the number of seats increases the aircraft weight and hence the required lift, L. Minimizing the amount of fuel burnt requires that we minimize the product of the required thrust of the engines and the duration of flight. Hence we wish to maximize the function

$$\mathcal{R}(T) = \frac{M_\infty L}{T} \tag{4.1}$$

where M_∞ is the freestream Mach number ($\sim \frac{1}{Duration}$), T is the total required thrust output from the engines and $\mathcal{R}$ is defined, here, to be the **"Range Parameter"**.

4.1 The Range Parameter & Single Point Objective Function

Assuming no thrust vectoring, the required thrust of the engines, T, is that which is needed to balance the total drag, D, of the aircraft. We wish to maximize the range parameter which is a function of D given by

$$\mathcal{R} = \frac{M_\infty L}{D} \tag{4.2}$$

Equation 4.2 is a form of the Breguet range equation where the rate of fuel consumption has been fixed and the change in aircraft weight ignored. [1] Note, the aim is not to maximize true range but, instead, minimize the total amount of fuel burned over the flight.

[1] In actuality, neither the rate of fuel consumption nor the aircraft weight are constant over the duration of a typical flight. As the aircraft design process matures the objective function should be altered to more closely reflect the goal.

In optimization it is traditional to solve for a minimum than a maximum. Here we define the inverse of the range parameter, $\mathcal{F} = \frac{1}{\mathcal{R}}$, as

$$\boxed{\mathcal{F} = \frac{D}{M_\infty L}} \tag{4.3}$$

It is this function that is of primary importance in this report and is referred to as the "**Single Point Objective Function**".

Chapter 5

The Physical Problem

5.1 3D Flow Over the OAW

The real problem can be broken down into separate, modelable, problems and the flow patterns around the wing classified. Refer to fig 5.1.

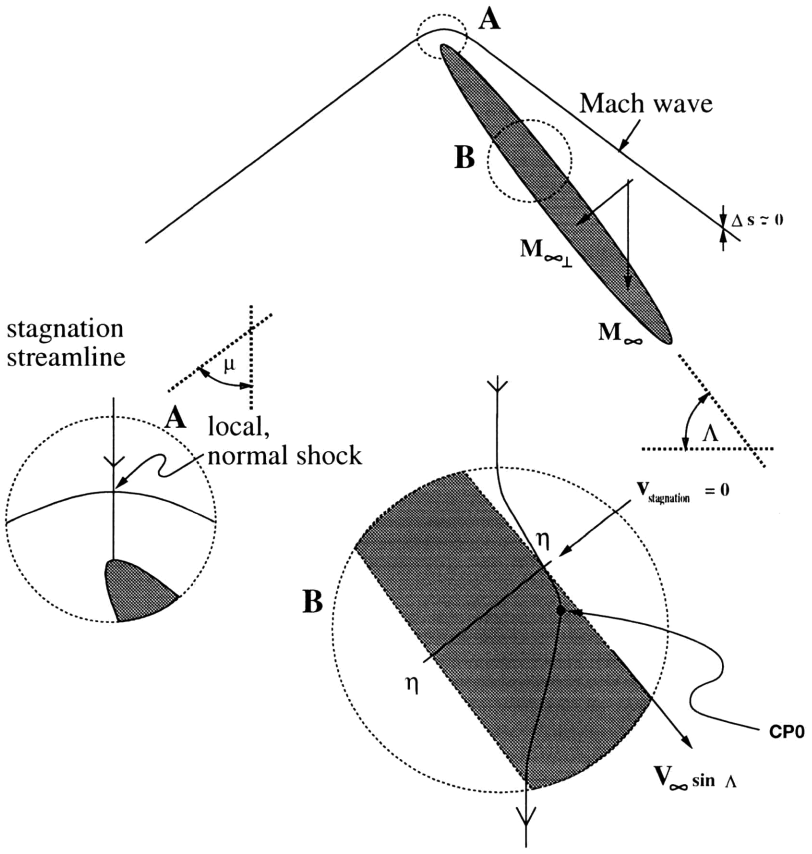

Figure 5.1: OAW Flow

The sweep angle, Λ, perpendicular components of freestream Mach number and velocity ($M_{\infty_\perp}$ & $V_{\infty_\perp}$ respectively) are defined in figure 5.1. Except for a very localized region, A, around the leading tip, the general flow pattern will be similar to that shown by B. Sub-figure B shows a streamline traced from the freestream. This can be explained as follows: For a wing of high axis ratio the leading edge is roughly parallel to the major axis. Also, the wing can be assumed cylindrical and hence the velocity component parallel to the major axis, $V_\infty \sin\Lambda$, will remain unaltered. In particular, the stagnation line near the leading edge has a zero perpendicular component and slides axially at $V_\infty \sin\Lambda$. This situation occurs due to the influence of the perpendicular pressure field created by the airfoil. Velocities in this direction are always subsonic by virtue of the wing being swept behind the leading tip Mach cone. Point $CP0$ maps to the airfoil and perpendicular section pressure coefficient plot as shown (fig. 5.2). At this point,

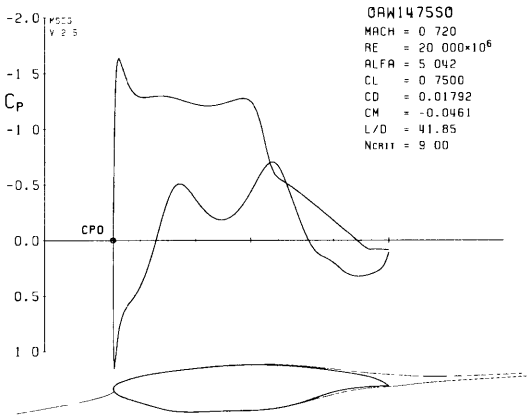

Figure 5.2: Velocity & Pressure Mapping of Traced Streamline

$C'_{P_\perp} = 0$, the magnitude of the streamline velocity must be that of the freestream since the axial component remains the same. Although significant spanwise flow will typically occur in the boundary layers, this will not couple significantly to the normal-direction boundary layer flow if the spanwise gradient of the spanwise flow is small (i.e. if the axis ratio is large) [24]. Modeling the problem this way allows decoupling of the 2D profile drag from the 3D effects.

5.2 Limitations & Approximations of the Physical Model

The wing is assumed to be "thin" with a high axis-ratio ($\geq$ 10) and be of elliptic planform. Transition to turbulent flow is expected to occur early on (at around 5% perpendicular chord[1]) and is independent of sweep. No attempt has been made to quantify the drag generated by the engines.

Away from the tip bow shock the airflow passes through the wave isentropically. The model assumes that the wave drag generated by the leading wing tip normal shock is insignificant compared with the total drag and so is ignored.

For the purpose of analyzing wave drag due to volume, the area distributions formed by cutting the wing with oblique Mach planes were assumed to be of the Sears-Haack type. This, however, implies a reduction in τ towards the wing tips that was not incorporated in this report. The error here is insignificant, with respect to other approximations, for an ellipse of high axis ratio.

For the purpose of the profile drag, the model assumes that perpendicular airfoil sections are similar at different geometric spanwise locations (different η values) and that, locally, the wing is approximately cylindrical (reasonable assumptions for high axis ratios.) In this case, the flow along the major axis of the wing is inconsequential (except for friction forces) and the flow problem can be considered in the perpendicular direction only – the components are resolved afterwards.

[1]Transition can be tripped by the user and is set by MSES input files. See section7.2.

Chapter 6
Method Procedure

6.1 The Accumulated Objective Function

Considering only a single point optimization procedure, the function to be minimized would be the single point objective function,

$$\mathcal{F} = F_{WI} + F_{W_{vol}} + F_F + F_P + F_{S_P} \tag{6.1}$$

where

$$\mathcal{F}_i = \frac{D_i}{M_\infty L} \tag{6.2}$$

for example

$$F_{WI} = \frac{D_{WI}}{M_\infty L} \quad etc.$$

In formulating the equations of 6.2, M_∞ is specified and the value of D determined by the methods detailed in chapter 7. The Lift, L, is calculated by MSES[25]. MSES operates with the local perpendicular section-lift coefficient , $C'_{L_\perp}$, the parameters $\rho_\infty, V_{\infty_\perp}$ and the geometry based upon $c(\eta)$. The density of the freestream is given by ρ_∞. Parameters, $V_{\infty_\perp}$ and $c(\eta)$ are defined as in figure 7.7. Hence, the lift is given by

$$L = \frac{1}{2}\rho_\infty {V_{\infty_\perp}}^2 \int_{-\frac{\tilde{b}}{2}}^{\frac{\tilde{b}}{2}} C'_{L_\perp} c(\eta)\, d\eta \tag{6.3}$$

$$= \frac{1}{2}\rho_\infty {V_{\infty_\perp}}^2 S C_{L_\perp} \tag{6.4}$$

to very good approximation. This assumes that $C_{L_\perp} = C'_{L_\perp}$ which is reasonable for large values of axis ratio, σ.

Single point optimization, however, does not prove practical. It invariably results in strictly localized minimization accompanied by heavily penalized off-design conditions.

Instead, the **accumulated objective function**, F_O, is minimized where

$$F_O = \sum_{n=1}^{N} w_n \mathcal{F}(n) \tag{6.5}$$

with N being the total number of operating points and w_n being the relative point-weighting parameters. In equation 6.5 the detailing of w_n is not specified. Weightings can be applied to differentiate between sets[1] of operating points as well as scaling the individual operating points within a set. The magnitude of F_O is arbitrary – only its turning point is relevant. An example summation for F_O is given below and refers to figure 6.1. Four perpendicular Mach numbers, $M_{\infty_\perp}(k)$, are considered together with eight freestream Mach numbers, $M_\infty(j)$, for each $M_{\infty_\perp}$ value. This is intended to capture the merit of the airfoil over a reasonably broad range of operating parameters.

For j sets (curves) and for k points in each set

$F_O = 0$

begin loop 1, $j = 1$ to 8

    $M_\infty = M_\infty(j)$

    begin loop 2, $k = 1$ to 4

        $M_{\infty_\perp} = M_{\infty_\perp}(k)$

        calculate $\mathcal{F}$

        $F_O = F_O + \mathcal{F}$

    end loop 2

end loop 1

The procedure used to obtain the airfoil geometry involves the use of the optimization driver LINDOP (see chapter 8) coupled with the non-linear flow solver MSES (see section 7.2.1). For a given airfoil geometry MSES will determine the flow properties and force and moment coefficients, together with their first order derivatives (sensitivities). LINDOP reads this flow sensitivity information and combines it with calculations determined by luser.f[2] and its subroutines (in this case 'OAW.f'[3]) to generate F_O and

[1] individual sets lie on individual curves of figure 6.1.

[2] see appendix C.

[3] see appendix D.

its vector of function sensitivities. The user may set constraints at this point. LINDOP then allows free parameters to be perturbed in such a way that their combined linear extrapolations reduce the value of F_O. Usually, the perturbations consist of airfoil deformations. Provided the perturbation step size is small enough, the generated new airfoil geometry, when fed back into MSES, will create coefficients similar to LINDOP's prediction. This cycle is then iterated until F_O reaches its minimum. The following example should clarify the procedure.

6.2 Procedure Example

- Running MSES

  1. The RAE 2822 airfoil (with scaled thickness) was used as the initial guess profile.
  2. ${C_{L_\perp}}'$ was fixed at 0.65.
  3. Four cases were specified; $M_{\infty_\perp} = 0.65, 0.70, 0.73$ and 0.75.
  4. MSES was executed producing four sets of output.

- Running LINDOP

  1. Activate/freeze parameters
     - Free-up airfoil incidence, ALFA
     - Free-up MODE-SHAPES
     - Fix M_∞ user variables
  2. Impose/remove constraints
     - Fix NOSE ANGLE = 180.0°
     - Fix pitching moment coefficient, $C_m = -0.05$
     - Fix $C'_{L_\perp} = 0.65$
     - Fix thickness constraint, $T1$ = .14c@.25c
     - Fix thickness constraint, $T2$ = .14c@.60c
  3. Begin a line descent (initially only)

4. Take a small step (in multi-parameter space)

5. Save new airfoil geometry

This procedure was repeated until the solution converged to tolerance. An F_O convergence history of several line descents is plotted in figure 6.2.

Figures 10.1 and 10.2 show the comparison between example initial and final airfoils with their accompanying pressure distributions.[4] The exact procedure used to create this airfoil involved a fair degree of 'hand-holding'. The hiccups and rectifications are detailed in the conclusions section of this report. Figure 6.3 overlays the initial and final airfoil geometries.

[4] this particular example had constraints different to the example specified in this section.

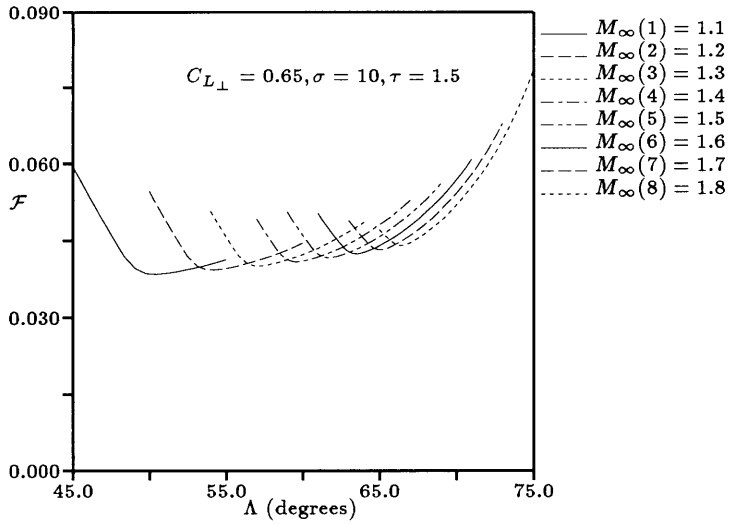

Figure 6.1: Example Optimization Points

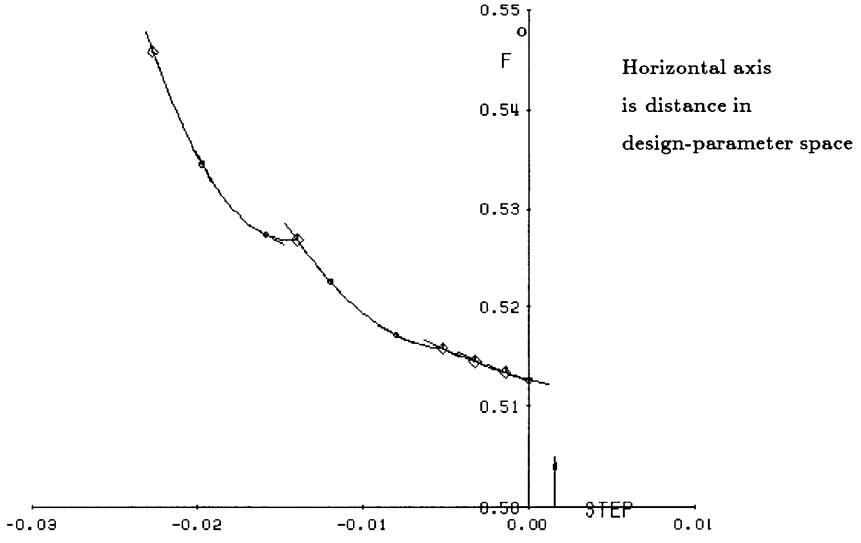

Figure 6.2: Sample F_O Convergence History

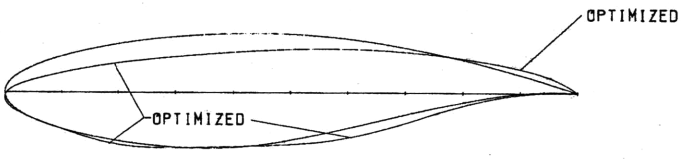

Figure 6.3: Initial & optimized airfoil geometries

Chapter 7
Drag Components

To minimize $\mathcal{F}(D, M_\infty, L)$ for a given freestream Mach number (based on engine requirements and speed desired) and lift (determined by payload requirements), we wish to minimize the drag. The method in this report splits up the total drag as follows

$$D = D_{WI} + D_{W_{vol}} + D_F + D_P + D_{S_P} \tag{7.1}$$

where

- D_{WI} = Wave drag due to lift and induced drag (3D, inviscid) - see section 7.1.1
- $D_{W_{vol}}$ = Wave drag due to volume (3D, inviscid) - see section 7.1.2
- D_F = Friction drag on airfoil (2D) - see section 7.2.3
- D_P = Pressure drag on airfoil (2D) - see section 7.2.4
- D_{S_P} = Drag as a result of reacting the side force – see section 7.3

Note: D_{WI} is the wave drag of the leading shock cone only. It does not include any possible shock along the wing itself that occurs if the perpendicular flow component over the wing becomes transonic - this would be included in D_P which is output from MSES.

7.1 Analytical Model of 3D Drag (Wave & Induced)

This section describes the analytical solutions to the wave and induced drag that were incorporated in the user function, 'OAW.f'. The models used were based on the linear supersonic small-disturbance theory of Jones[26] and limited to thin wings – though this limit was one for simplicity only. For a general model describing inviscid drag of supersonic configurations see reference [27].

Provided that perturbations in the z-direction remain small compared to the flight direction, linear theory provides a very good approximation of the flow field around a thin wing. The airfoil section of the OAW is likely to be thicker than a typical airfoil section of a civil airliner wing in order to accommodate passengers but the approximation of "thin wing theory" is still appropriate, particularly with increasing sweep. Under linear approximations the drag due to lift may be separated from the drag due to volume. This report analyses the drag of a swept oblique wing of "to be determined" airfoil section. The drag due to lift for this planform is described in section 7.1.1. The drag due to volume is described in section 7.1.2 **for an airfoil of optimum thickness distribution**[1]. Whilst a better model (based on the variable mode shapes) could have been calculated (for instance by the method described by Ashley & Landahl [27] chp.9) the differences are small so were not incorporated.

The following sections of this chapter can be summarized as follows.

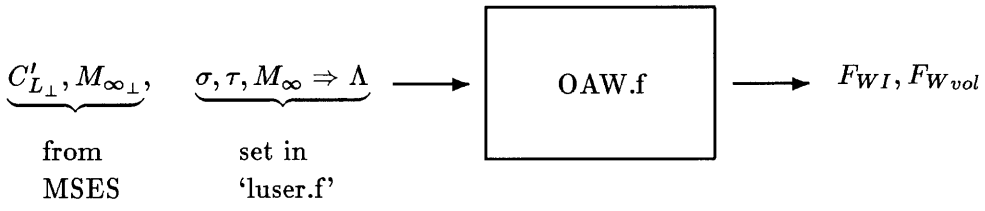

σ and τ are defined in sections 7.1.1 and 7.1.2, respectively.

[1] The airfoil was modeled as a bi-convex parabolic lens with a central point of maximum thickness.

7.1.1 Inviscid Drag due to lift, D_{WI} (Wave and Induced)

Jones [2, 28] shows that for minimum inviscid drag due to lift (i.e., that due to lift dependent wave drag combined with induced drag) the distribution of lift should be such that the induced downwash is uniform. This can be achieved by a distribution of lift elliptic both in the streamwise and spanwise directions. The simplest construction of this is an oblique "lifting line" positioned such that it lies within the Mach cone generated by the leading tip. See Figure 7.1. Physically, this lifting line could represent a wing of extremely high axis ratio, σ, where again referring to figure 7.4

$$\sigma = \frac{\tilde{b}}{\tilde{c}}$$

and in this case $\tilde{c} \to 0$. The drag due to lift for this lifting line, D_{ll}, is given below.

$$D_{ll} = \frac{1}{\sqrt{1-m^2}} \frac{L^2}{\pi q_\infty Y^2} \tag{7.2}$$

where

$$m = \frac{Y}{y_\mu} \tag{7.3}$$

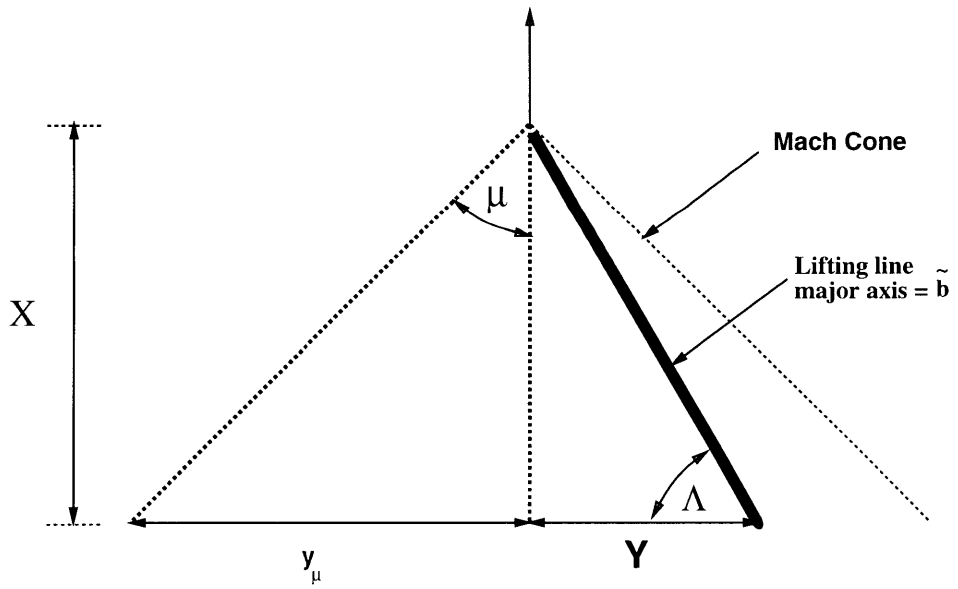

Figure 7.1: Drag of Oblique Lifting Line

Assuming the lift to be distributed uniformly over a high aspect ratio elliptic planform of axis ratio σ, and writing in terms of sweep angle, axis ratio and freestream Mach number the drag is given by

$$D_{ll} = \frac{L^2}{\pi q_\infty \tilde{b}^2} \frac{\tan\Lambda(1+\tan^2\Lambda)}{\sqrt{\tan^2\Lambda - ({M_\infty}^2 - 1)}} \tag{7.4}$$

where $\tilde{b}$ is defined in figure 7.1 This gives the "to be minimized" function, F_{ll}, as

$$F_{ll} = \frac{D_{ll}}{M_\infty L} = \frac{C_L}{4M_\infty \sigma} \frac{\tan\Lambda(1+\tan^2\Lambda)}{\sqrt{\tan^2\Lambda - ({M_\infty}^2 - 1)}} \tag{7.5}$$

Figure 7.2 shows this trend in F_{ll} for a sequence of freestream Mach numbers at fixed $C_L = 1$ and $\sigma = 10$. Where C_L is the true lift coefficient $= \frac{L}{\frac{1}{2}\rho_\infty {V_\infty}^2 S}$.

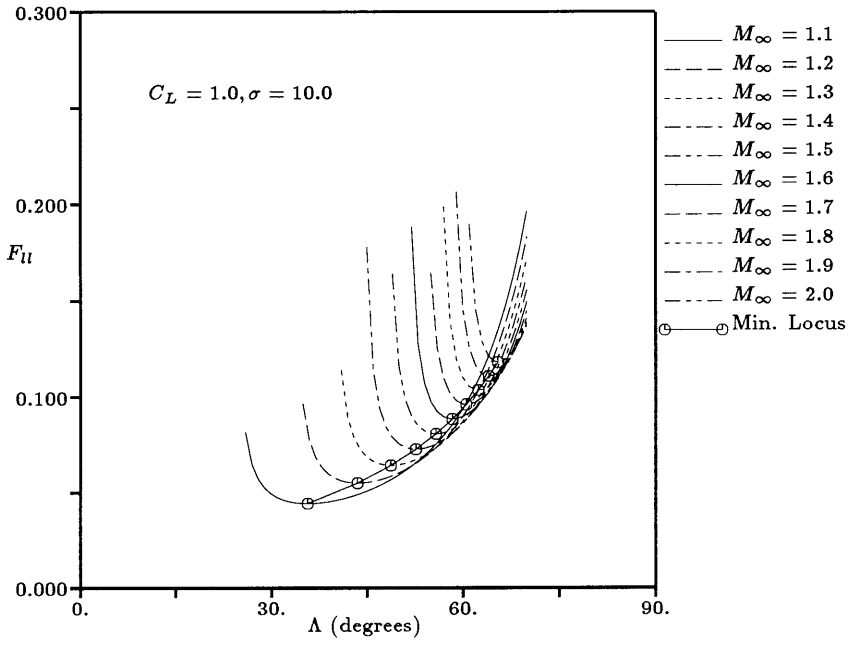

Figure 7.2: F_{ll} vs Λ for the Supersonic Oblique Lifting Line

To maintain the same value of lift at the different freestream Mach numbers and fixed C_L, the value of ρ_∞ is assumed to vary. i.e., the aircraft changes altitude as needed. The locus of minima, $\frac{\partial F_{ll}}{\partial \Lambda} = 0$, is given by

$$F_{llmin} = F_{llmin}(\Lambda_{opt})$$

where

$$\Lambda_{opt} = \arctan\left\{\frac{1}{2}\sqrt{3\beta^2 + \sqrt{\beta^2(9\beta^2+8)}}\right\} \tag{7.6}$$

and

$$\beta = \sqrt{{M_\infty}^2 - 1} \tag{7.7}$$

This locus is also plotted suggesting the optimum angle of sweep such as to minimize F_{ll}. This function holds only for the case where the lifting-line is swept behind the Mach cone i.e., when the component of the freestream velocity perpendicular to the lifting-line remains subsonic ($M_{\infty\perp} < 1$). Hence the curves of Figure 7.2 begin at $\Lambda = (90° - \mu)$. For a given freestream flight Mach number, the portion of the curve to the left of the minimum pays the penalty with respect to wave drag (which favors a high sweep) whilst the portion to the right suffers more induced drag due to the reduced aerodynamic aspect ratio.

A more practical way to achieve the minimum-drag lift distribution is by way of a uniform lift distribution over an elliptic planform. A model for the oblique ellipse was later given by Jones [28, 26] in the form

$$C_{D_{WI}} = \frac{{C_L}^2}{4}\Re[\beta^2 - (m' + i\frac{a'}{b'})]^{\frac{1}{2}} \tag{7.8}$$

and the notation defined in Figure 7.4. Written in terms of sweep angle, axis ratio and freestream Mach number

$$\boxed{D_{WI} = \frac{L^2\sigma}{q_\infty \tilde{b}^2\pi}\Re[Z_1]} \tag{7.9}$$

and the "to be minimized" function is given by

$$\boxed{F_{WI} = \frac{C_{L_\perp}\cos^2\Lambda}{4M_\infty}\Re[Z_1]} \tag{7.10}$$

where, again referring to Figure 7.4

$$Z_1 = [\beta^2 - (m' + in)]^{\frac{1}{2}} \tag{7.11}$$

$$\beta^2 = {M_\infty}^2 - 1 \tag{7.12}$$

$$m' = \frac{(\sigma^2 - 1)\sin\Lambda\cos\Lambda}{\sin^2\Lambda + \sigma^2\cos^2\Lambda} \tag{7.13}$$

$$n = \frac{\sigma}{\sin^2\Lambda + \sigma^2\cos^2\Lambda} \tag{7.14}$$

Writing Z_1 in the form $Z_1 = \left(re^{i\theta}\right)^{\frac{1}{2}} = \sqrt{r}(\cos\frac{\theta}{2} + \sin\frac{\theta}{2})$ gives

$$\Re\{Z_1\} = \sqrt{r}\cos\frac{\theta}{2} \tag{7.15}$$

where

$$\theta = \arctan\left\{(-2m'n), (\beta^2 + n^2 - m'^2)\right\} \tag{7.16}$$

$$r = \sqrt{4m'^2n^2 + (\beta^2 + n^2 - m'^2)^2} \tag{7.17}$$

The function F_{WI}, expressed in the form of equations (7.10) and (7.15) is incorporated in the subroutine 'OAW.f'. Figure 7.3 shows an example plot of F_{WI} against sweep angle for a wing of axis ratio, $\sigma = 10$ and a lift coefficient of $C_L = (C_{L_\perp}\cos^2\Lambda) = 1$.

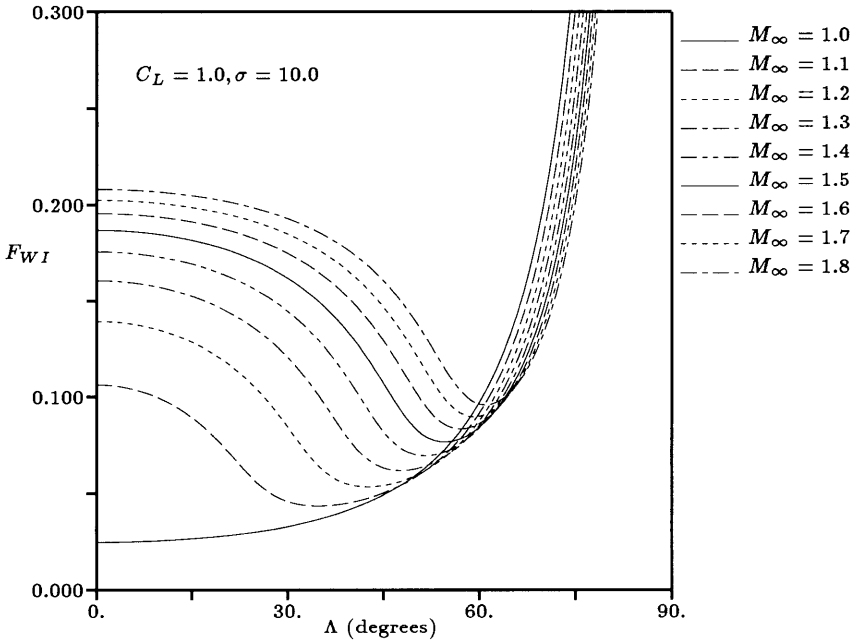

Figure 7.3: F_{WI} vs Λ for the Supersonic Oblique Ellipse

Keeping C_L constant shows the drag "bucket" resulting from the trade-off between wave drag due to lift and induced drag. The optimization procedure will set $C_{L_\perp} =$ *constant* which is why the shape of F_{WI} differs from that observed in figure 7.11 shown later in section 7.4.

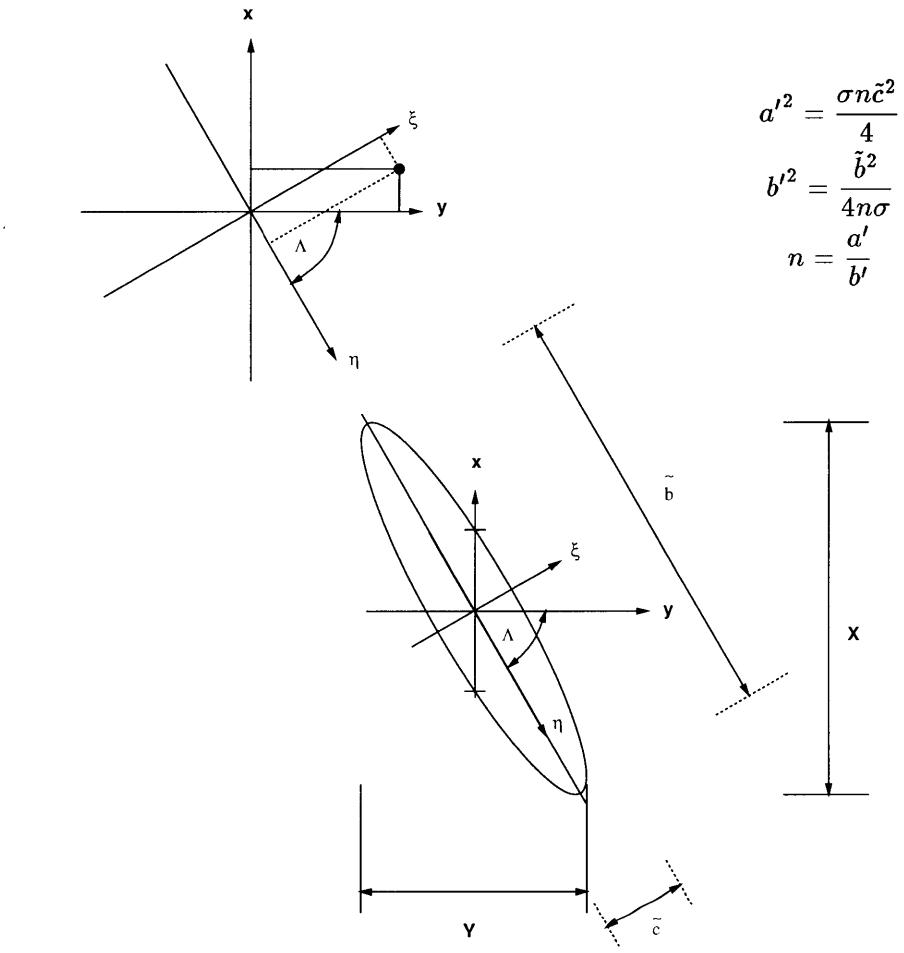

$$a'^2 = \frac{\sigma n \tilde{c}^2}{4}$$

$$b'^2 = \frac{\tilde{b}^2}{4n\sigma}$$

$$n = \frac{a'}{b'}$$

Figure 7.4: Oblique Elliptic Wing & Notation – Relations were derived by rotating the ellipse through the coordinate system shown & solving for turning points.

7.1.2 Inviscid Drag due to Volume, $D_{W_{vol}}$ (Wave)

The following model represents the wave drag due to volume of an oblique ellipse of **optimum airfoil section** – this being a bi-convex parabolic lens. This model was incorporated into the user function 'OAW.f'. Jones [26] showed that for a distribution of thickness, t, lying along the streamwise chord axis, x, the distribution, $\frac{\partial^2 t(\xi,\eta)}{\partial x^2} = constant$, yields the minimum drag for a given volume. Smith [29] found that for the planform configuration described by Figure 7.4, the optimum airfoil section is parabolic. In such a case the product of the streamwise chord length (which varies elliptically) with the parabolic thickness distribution leads to a volume distribution of the Sears-Haack type. The value of τ ($\tau = \frac{t_{max}}{c}$) is assumed to diminish at the wing-tips. Smith's result follows,

$$C_{D_{W_{vol}}} = \frac{t^2}{a'^2}\Re\left\{\frac{\beta^2 - (m' + i\frac{a'}{b'})(m' + 2i\frac{a'}{b'})}{[\beta^2 - (m' + i\frac{a'}{b'})^2]^{\frac{3}{2}}}\right\} \tag{7.18}$$

with notation defined as before (see Figure 7.4).

Alternatively, this can be written in the form,

$$C_{D_{W_{vol}}} = \frac{4\tau^2}{\sigma n}\Re\{Z_2\} \tag{7.19}$$

hence

$$\boxed{D_{W_{vol}} = \frac{q_\infty \tilde{b}^2 \pi \tau^2}{\sigma^3}(\sin^2\Lambda + \sigma^2\cos^2\Lambda)\Re\{Z_2\}} \tag{7.20}$$

thus giving the "to be minimized" function as

$$\boxed{F_{W_{vol}} = \frac{4\tau^2}{M_\infty C_{L_\perp}\sigma^2}(\tan^2\Lambda + \sigma^2)\Re\{Z_2\}} \tag{7.21}$$

where

$$Z_2 = \frac{\beta^2 - (m' + in)(m' + 2in)}{[\beta^2 - (m' + in)^2]^{\frac{3}{2}}} \tag{7.22}$$

$$\Re\{Z_2\} = \frac{1}{r^{\frac{3}{2}}}\left\{\phi\cos\frac{3\theta}{2} - 3\psi\sin\frac{3\theta}{2}\right\} \tag{7.23}$$

$$\phi = (\beta^2 + 2n^2 - m'^2) \tag{7.24}$$

$$\psi = m'n \tag{7.25}$$

with r and θ defined as before.

The function $F_{W\,vol}$, expressed in the form of equations (7.21) and (7.23) was incorporated in the subroutine 'OAW.f'. Figure 7.5 shows an example plot of $F_{W\,vol}$ against sweep angle for a wing of axis ratio, $\sigma = 10$, a lift coefficient of $C_L = (C_{L_\perp}\cos^2\Lambda) = 1$ and a maximum thickness/chord ratio of $\tau = 0.1$.

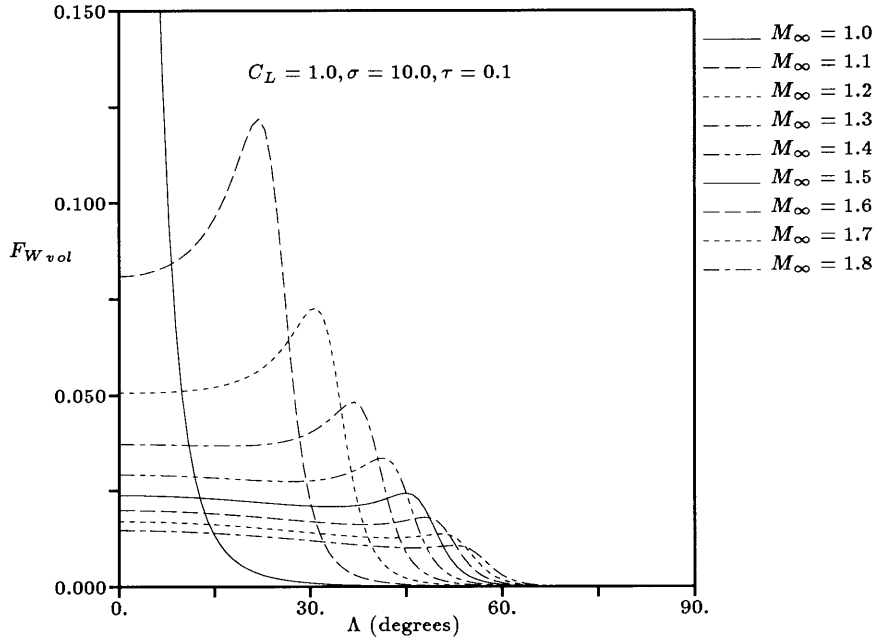

Figure 7.5: $F_{W\,vol}$ vs Λ for the Supersonic Oblique Ellipse

7.2 Numerical Model of 2D Drag (Airfoil Profile Drag)

The airfoil profile drag (that due to friction and pressure about the airfoil) was calculated using MSES [25, 30, 31] and its related supporting programs.

7.2.1 Briefing on the 2D Flow Solver, MSES

MSES[25] is a two dimensional multi-element airfoil design/analysis program that allows inverse design. The 2-D flow is modeled as a discrete number of streamtubes coupled through the position of, and pressure at, the streamline interfaces. The unknown variables are the density and the position of the streamlines. The discrete Euler equations are assembled as a system of nonlinear equations. The outer inviscid flow is solved by the Euler equations in conservative form and is thus capable of capturing shocks. Coupled integral boundary-layer analysis [30] handles the viscous effects. MSES reads and writes perpendicular quantities which are resolved along the axes of interest outside of the MSES environment. Figure 7.6 below shows a streamline grid resulting from a calculation. Due to the high Reynolds number typical on large transport aircraft,

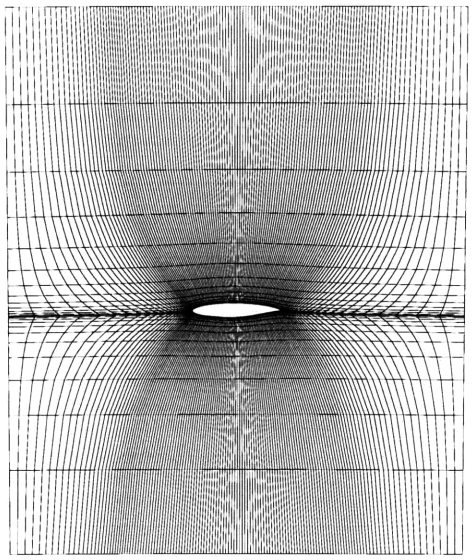

Figure 7.6: Typical Control Volume used by MSES

the boundary layer is assumed to be turbulent from roughly 5% chord onwards and is tripped accordingly[2]. The top and bottom-most streamlines are six chords apart, the side boundaries are set two chords upstream and downstream. The farfield potential is determined from the Prandtl-Glauert equation with the circulation constant defined by the imposed Kutta condition. This potential is used to impose pressure and flow angle boundary conditions on the domain perimeter. The boundary layer or wake displacement thickness determines the position of the inner-most inviscid streamline, this being the airfoil surface and wake boundary condition. The wake also has constant pressure imposed across it. A key feature of MSES is its ability to very efficiently generate sensitivities of flow quantities (such as $C_{L_\perp}, C_{D_\perp}$, etc.) to geometry perturbations. These sensitivities are then used in LINDOP to perform optimization changes to the design. The MSES/LINDOP cycle is shown below:

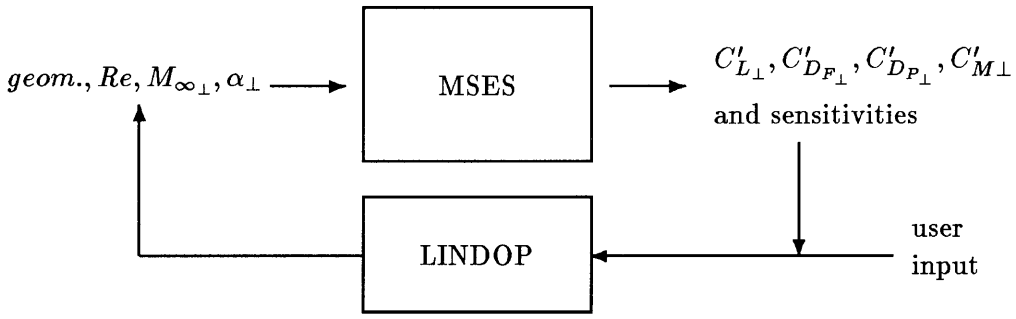

MSES operates with section force coefficients (shown primed) in the perpendicular direction (shown by perpendicular subscript). Throughout this report, due to expected high values of σ, section coefficients are assumed equal to the wing coefficients eg. $C_{L_\perp} = C'_{L_\perp}$. The drag coefficients are defined in sections 7.2.3 and 7.2.4. $C'_{M\perp}$ is the perpendicular section moment coefficient

$$C'_{M\perp} = \frac{P_M}{\frac{1}{2}\rho_\infty {V_\infty}_\perp{}^2 S} \tag{7.26}$$

where P_M is the pitching moment about the major axis.

[2] turbulence was tripped @ 5% on the pressure surface & @ 2% on the suction surface.

7.2.2 Lift Coefficients - 2D and 3D

The objective function, $\mathcal{F}$, is dependent upon several variables. Constraints fix some and create dependencies with others. It is convenient to relate the true lift coefficient, C_L, to the perpendicular lift coefficient, $C_{L_\perp}$. Analysis in both freestream and perpendicular

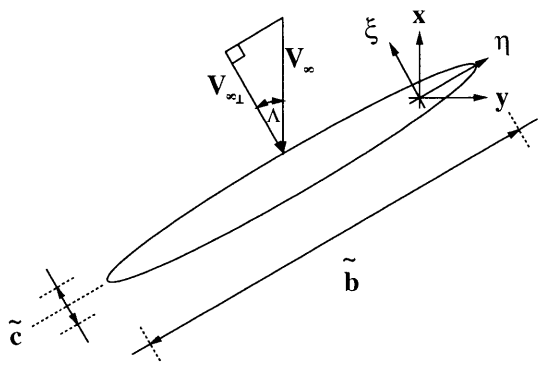

Figure 7.7: The Effect of Axes Rotation on C_L and $C_{L_\perp}$

coordinates of the components that comprise the lift, gives the following equation

$$L = \frac{1}{2}\rho_\infty {V_\infty}^2 S C_L = \frac{1}{2}\rho_\infty {V_{\infty_\perp}}^2 S C_{L_\perp} \tag{7.27}$$

From figure 7.7 and equation 7.27

$$V_{\infty_\perp} = V_\infty \cos\Lambda \tag{7.28}$$

$$M_{\infty_\perp} = M_\infty \cos\Lambda \tag{7.29}$$

$$C_L = C_{L_\perp} \cos^2\Lambda \tag{7.30}$$

7.2.3 Profile Friction Drag, D_F

Skin friction is a function of S, q_∞, M_∞ and transition location. At high Reynolds numbers transition occurs very early on (typically first rivet line) and so is set in MSES

to trip at around 5% of the chord. In such a case, the friction drag is largely independent of sweep, giving

$$D_F = \frac{1}{2}\rho_\infty {V_\infty}^2 S C_{D_{F_\perp}} \tag{7.31}$$

where $C_{D_{F_\perp}}$ is the perpendicular coefficient of drag due to friction. Due to large values of σ, $C_{D_{F_\perp}} = C'_{D_{F_\perp}}$ (the coefficient that MSES operates with). The coefficient $C_{D_{F_\perp}}$ has no directionality associated with it and is treated so. Fixing $C_{L_\perp}$, however, enforces a sweep dependence. Hence

$$\boxed{F_F = \frac{C_{D_{F_\perp}}}{M_\infty C_{L_\perp} \cos^2 \Lambda}} \tag{7.32}$$

7.2.4 Profile Pressure Drag, D_P

At any geometric spanwise location along the wing the forces set up by the flow can be resolved into the directions ξ, η and z. Due to the cylindrical shape of the wing and the similarity of spanwise (η direction) airfoil sections, the pressure force in the η direction is zero. Then L' acts in the z–direction and $D'_{P_\perp}$ in the ξ–direction (where primes refer to section force coefficients). Refer to figure 7.8 which shows the total forces summed over the sections. The perpendicular total drag due to pressure has been resolved into the true drag and side-force due to pressure, D_P and S_P respectively [3].

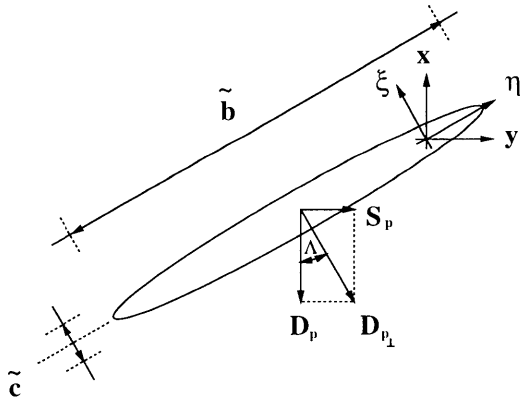

Figure 7.8: The Effect of Axes Rotation on D_P

[3] the side-force is dealt with in section 7.3.

$$D_P{}'_\perp = \frac{1}{2}\rho_\infty {V_\infty}_\perp{}^2 c(\eta) C'_{D_{P_\perp}} \tag{7.33}$$

$$D_P = 2\int_0^{\frac{b}{2}} D_P{}'_\perp \, d\eta \cos\Lambda = \frac{1}{2}\rho_\infty {V_\infty}_\perp{}^2 S C_{D_{P_\perp}} \cos\Lambda \tag{7.34}$$

giving

$$\boxed{F_P = \frac{C_{D_{P_\perp}} \cos\Lambda}{M_\infty C_{L_\perp}}} \tag{7.35}$$

7.3 Side-force, S_P, and associated drag, D_{S_P}

Due to the antisymmetric configuration of the wing a side-force results. The component of $D_{P_\perp}$ in the y direction results in a side-force, S_P. Two options were considered to the method of reacting this side-force – namely vectoring the jet efflux or using aerodynamic forces via vertical control surfaces. In either case, a drag penalty will be paid. The two options are detailed below. The subroutine, 'OAW.f', incorporated the aerodynamic control surface option with an assumed side-force/drag ratio, α_{S_P}, of 20. Referring to figure 7.8.

$$\frac{S_P}{M_\infty L} = \frac{C_{D_{P_\perp}} \sin\Lambda}{M_\infty C_{L_\perp}} \tag{7.36}$$

Option 1: Define α_{S_P} to be $\frac{Side-force}{drag}$ ratio then

$$D_{S_P} = \frac{S_P}{\alpha_{S_P}} \tag{7.37}$$

hence

$$\boxed{F_{S_P} = \frac{C_{D_{P_\perp}} \sin\Lambda}{M_\infty C_{L_\perp} \alpha_{S_P}}} \tag{7.38}$$

Option 2: Loss in engine thrust due to Vectoring. For the purpose of this section the term E will be defined as the thrust **of the engines** and the **loss** in true thrust will be viewed as an additional drag, D_ϵ. i.e., take the pilot's view point; he does not see the obliqueness of the engines, he just experiences a change in thrust demand. Also note, for this section only, that

$$D = D_{WI} + D_{W_{vol}} + D_F + D_P \tag{7.39}$$

and the required thrust balances the effective drag, $\mathcal{D}$, where

$$\mathcal{D} = D + D_\epsilon \tag{7.40}$$

We now wish to maximize the range equation which is now a function of $\mathcal{D}$, given by,

$$\mathcal{R} = \frac{M_\infty L}{\mathcal{D}} \tag{7.41}$$

Determination of D_ϵ (refer to figure 7.9):

$$E \sin\epsilon = S_P \tag{7.42}$$

$$E \cos\epsilon = D \tag{7.43}$$

therefore

$$D_\epsilon = E - D = \sqrt{D^2 + {S_P}^2} - D \tag{7.44}$$

ie.

$$F_{vec} = \frac{\sqrt{D^2 + {S_P}^2} - D}{M_\infty L} \tag{7.45}$$

The choice of actual method to be adopted by the aircraft manufacturer involves many deciding factors. The inclusion here was for completeness and interest sake. Figure 7.11 shows the insensitivity to airfoil choice. The drag magnitudes of the two methods, plotted in fig. 7.10, suggest that drag minimization may not be the deciding factor in choosing the side-force reacting mechanism.

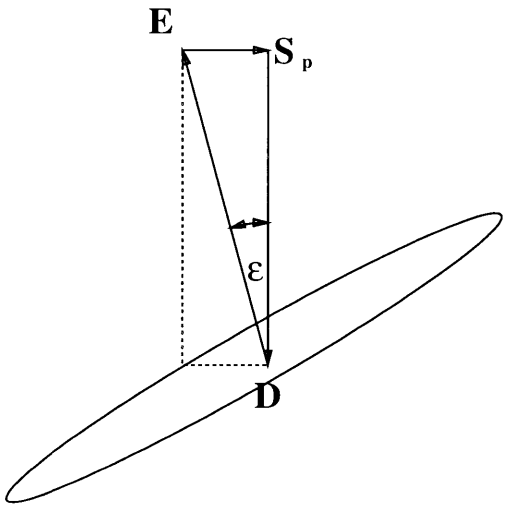

Figure 7.9: Vectored Thrust and Generated Drag

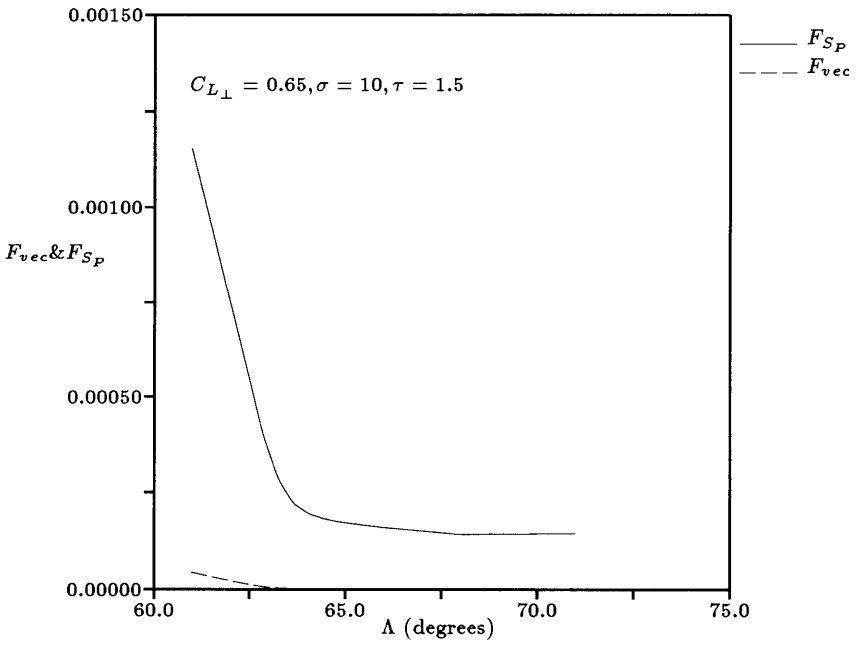

Figure 7.10: F_{vec} & F_{S_P} Comparison

7.4 Comparison of Individual Drag Components

To give a feel for the relative importance of the individual components of D, figure 7.11 shows the breakdown – expressed in terms of $\mathcal{F}_i$ – at a single freestream Mach number.

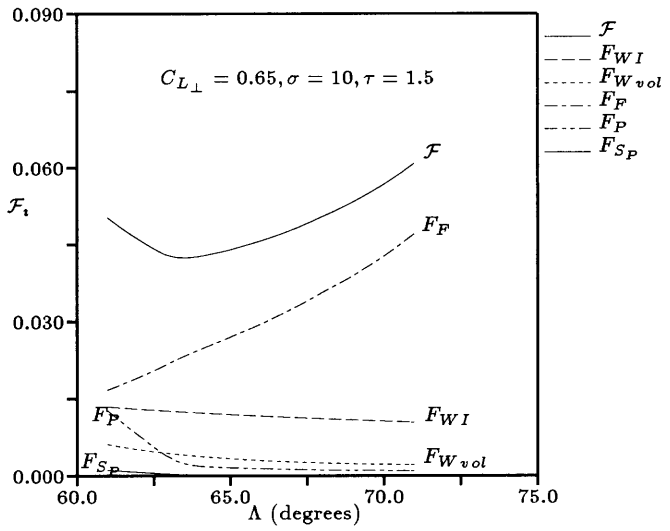

Figure 7.11: Comparison of Individual Drag Components (Expressed in Terms of $\mathcal{F}_i$) at $M_\infty = 1.6$

The surprising insensitivity of the 3D drag components is explained in the Conclusions section of this report.

Chapter 8
Briefing on the optimization Procedure, LINDOP

This section briefs the user on some of the mechanisms of LINDOP. Greater detail about LINDOP can be found in reference [1].

MSES and LINDOP work together to converge upon a desirable airfoil. LINDOP steers the direction by calculating linear extrapolations of parameters, including the airfoil geometry, so as to reduce the defined objective function. Within the LINDOP environment the user may hold parameters fixed and allow others to vary. For instance, the pitching moment coefficient may be constrained during a linear optimization step. LINDOP will then allow the other variables to float so as to reduce the objective function under the new conditions. There exists a solid body rotational degree of freedom[1] to allow the incidence of the airfoil to be controlled/freed which, of course, has its effect upon $C'_{L_\perp}$. The airfoil surface-geometry perturbations are achieved by expressing the airfoil with a finite number of Chebyshev mode shapes, say 17, and allowing each to vary, within defined constraints, so as to achieve the previously stated objective. A plot of these mode shapes is given in figure 8.1.

After any perturbation of the airfoil geometry and/or parameters (i.e. $C'_{L_\perp}, M_\infty$ & Λ) the new drag values are calculated in MSES and the cycle continued until satisfactory convergence has been achieved.

[1] in the single element case incorporated by this report this DOF is represented by $\alpha_\perp$, the airfoil incidence.

8.1 LINDOP subroutines 'luser.f' & 'OAW.f'

LINDOP and MSES work only with airfoil (2D) coordinates and parameters. Subroutine 'OAW.f' reads in the output from MSES, resolves the coefficients into the true flight direction and calculates the individual components of the single point objective function together with their sensitivities.[2] In this routine the functional relationship is

$$\mathcal{F} = \mathcal{F}(M_\infty, \Lambda, C_{L_\perp}, C_{D_{F_\perp}}, C_{D_{P_\perp}}) \tag{8.1}$$

The perpendicular parameters are those which have been calculated by MSES. M_∞ is defined from the list of user parameters and Λ is calculated in subroutine 'luser.f' on the basis that

$$M_{\infty_\perp} = M_\infty \cos\Lambda \tag{8.2}$$

$M_{\infty_\perp}$ having been defined for the separate MSES runs (refer to section 6.1 and figure 6.1).

Then, the individual sensitivities output from 'OAW.f' are with respect to the five functional parameters of equation 8.1. Subroutine 'luser.f' accumulates the $\mathcal{F}_i$'s and their derivatives, only now the functional parameter Λ has been replaced with $M_{\infty_\perp}$.

[2] refer to chapters 7 and 9 for the mathematical formulations used within 'OAW.f'.

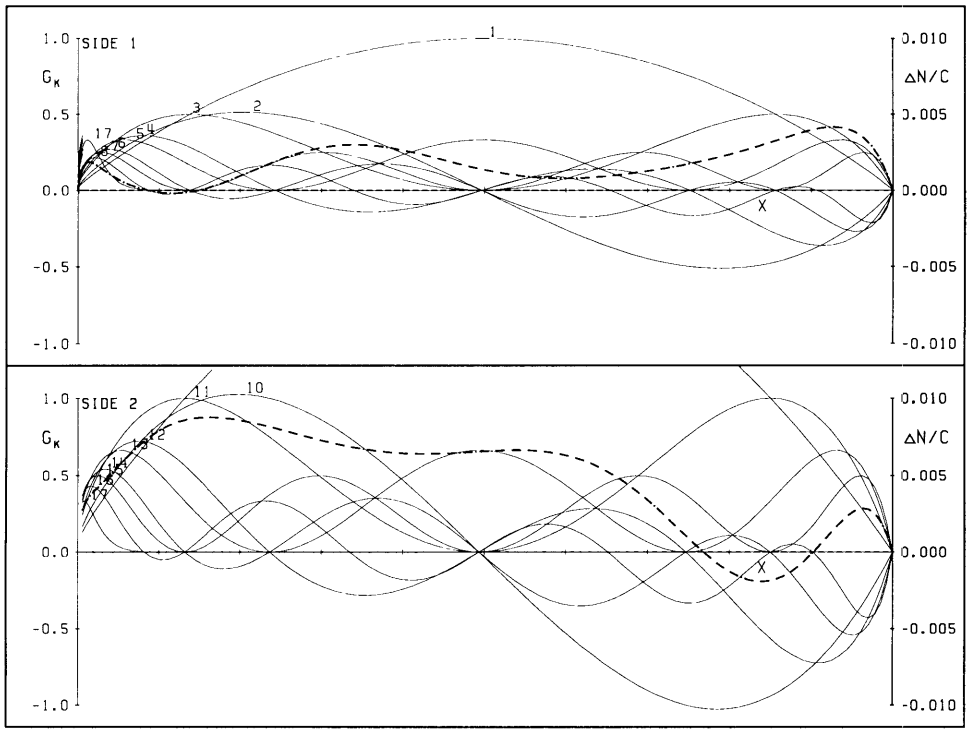

Figure 8.1: Airfoil surface deformation mode shapes

Chapter 9

Objective Function and its Sensitivities

9.1 The 'F' Equations & their Functional Relationships

This chapter expresses the mathematical functional relationships of the individual components that comprise the single point objective function calculated in subroutine 'OAW.f'. The functional dependence upon airfoil geometry is hidden within the three perpendicular force coefficients which, on entry to 'OAW.f' will have been calculated by MSES. The functional dependence upon Λ is later replaced with that of $M_{\infty_\perp}$ in subroutine 'luser.f'.

$$\begin{aligned} \mathcal{F} &= \mathcal{F}(M_\infty, \Lambda, C_{L_\perp}, C_{D_{F_\perp}}, C_{D_{P_\perp}}) \\ \mathcal{F} &= F_{WI} + F_{W\,vol} + F_F + F_P + F_{S_P} \end{aligned} \tag{9.1}$$

$$\begin{aligned} F_{WI} &= F_{WI}(M_\infty, \Lambda, C_{L_\perp}, r(M_\infty, \Lambda), \theta(M_\infty, \Lambda)) \\ F_{WI} &= \frac{C_{L_\perp}\cos^2\Lambda}{4M_\infty}\sqrt{r}(\cos\frac{\theta}{2}) \end{aligned} \tag{9.2}$$

$$\begin{aligned} F_{W\,vol} &= F_{W\,vol}(M_\infty, \Lambda, C_{L_\perp}, r(M_\infty, \Lambda), \theta(M_\infty, \Lambda), \phi(M_\infty, \Lambda), \psi(\Lambda)) \\ F_{W\,vol} &= \frac{4\tau^2}{M_\infty C_{L_\perp}\sigma^2}(\tan^2\Lambda + \sigma^2)\frac{1}{r^{\frac{3}{2}}}\left\{\phi\cos\frac{3\theta}{2} - 3\psi\sin\frac{3\theta}{2}\right\} \end{aligned} \tag{9.3}$$

$$\begin{aligned} F_F &= F_F(M_\infty, \Lambda, C_{L_\perp}, C_{D_{F_\perp}}) \\ F_F &= \frac{C_{D_{F_\perp}}}{M_\infty C_{L_\perp}\cos^2\Lambda} \end{aligned} \tag{9.4}$$

$$F_P = F_P(M_\infty, \Lambda, C_{L_\perp}, C_{D_{P_\perp}})$$

$$F_P = \frac{C_{D_{P_\perp}} \cos\Lambda}{M_\infty C_{L_\perp}} \tag{9.5}$$

$$F_{S_P} = F_{S_P}(M_\infty, \Lambda, C_{L_\perp}, C_{D_{P_\perp}})$$

$$F_{S_P} = \frac{C_{D_{P_\perp}} \sin\Lambda}{M_\infty C_{L_\perp}} \tag{9.6}$$

9.2 The 'F' Derivative Chain

$$\mathcal{F} = \mathcal{F}(M_\infty, \Lambda, C_{L_\perp}, C_{D_{F_\perp}}, C_{D_{P_\perp}})$$

$$\mathcal{F} = F_{WI} + F_{W\,vol} + F_F + F_P + F_{S_P} \tag{9.7}$$

$$\frac{\partial \mathcal{F}}{\partial M_\infty} = \frac{\partial F_{WI}}{\partial M_\infty} + \frac{\partial F_{W\,vol}}{\partial M_\infty} + \frac{\partial F_F}{\partial M_\infty} + \frac{\partial F_P}{\partial M_\infty} + \frac{\partial F_{S_P}}{\partial M_\infty} \tag{9.8}$$

$$\frac{\partial \mathcal{F}}{\partial \Lambda} = \frac{\partial F_{WI}}{\partial \Lambda} + \frac{\partial F_{W\,vol}}{\partial \Lambda} + \frac{\partial F_F}{\partial \Lambda} + \frac{\partial F_P}{\partial \Lambda} + \frac{\partial F_{S_P}}{\partial \Lambda} \tag{9.9}$$

$$\frac{\partial \mathcal{F}}{\partial C_{L_\perp}} = \frac{\partial F_{WI}}{\partial C_{L_\perp}} + \frac{\partial F_{W\,vol}}{\partial C_{L_\perp}} + \frac{\partial F_F}{\partial C_{L_\perp}} + \frac{\partial F_P}{\partial C_{L_\perp}} + \frac{\partial F_{S_P}}{\partial C_{L_\perp}} \tag{9.10}$$

$$\frac{\partial \mathcal{F}}{\partial C_{D_{F_\perp}}} = \frac{\partial F_F}{\partial C_{D_{F_\perp}}} \tag{9.11}$$

$$\frac{\partial \mathcal{F}}{\partial C_{D_{P_\perp}}} = \frac{\partial F_P}{\partial C_{D_{P_\perp}}} + \frac{\partial F_{S_P}}{\partial C_{D_{P_\perp}}} \tag{9.12}$$

Subordinate derivatives are documented in section 9.3.

9.3 Subordinate Derivatives

9.3.1 Primary Variables

9.3.1.1 $F_{WI}(M_\infty, \Lambda, C_{L_\perp})$

$$F_{WI} = \frac{C_{L_\perp}\cos^2\Lambda}{4M_\infty}\Re[Z_1] \tag{9.13}$$

$$\Re\{Z_1\} = \sqrt{r}\cos\frac{\theta}{2} \tag{9.14}$$

$$\frac{\partial(\Re\{Z_1\})}{\partial r} = \frac{\Re\{Z_1\}}{2r} \tag{9.15}$$

$$\frac{\partial(\Re\{Z_1\})}{\partial \theta} = \frac{-\Re\{Z_1\}\tan\frac{\theta}{2}}{2} \tag{9.16}$$

$$\frac{\partial F_{WI}}{\partial M_\infty} = F_{WI}\left[\frac{1}{\Re\{Z_1\}}\frac{\partial(\Re\{Z_1\})}{\partial M_\infty} - \frac{1}{M_\infty}\right] \tag{9.17}$$

$$\frac{\partial(\Re\{Z_1\})}{\partial M_\infty} = \frac{\partial(\Re\{Z_1\})}{\partial r}\frac{\partial r}{\partial M_\infty} + \frac{\partial(\Re\{Z_1\})}{\partial \theta}\frac{\partial \theta}{\partial M_\infty} \tag{9.18}$$

$$\frac{\partial F_{WI}}{\partial \Lambda} = F_{WI}\left[\frac{1}{\Re\{Z_1\}}\frac{\partial(\Re\{Z_1\})}{\partial \Lambda} - 2\tan\Lambda\right] \tag{9.19}$$

$$\frac{\partial(\Re\{Z_1\})}{\partial \Lambda} = \frac{\partial(\Re\{Z_1\})}{\partial r}\frac{\partial r}{\partial \Lambda} + \frac{\partial(\Re\{Z_1\})}{\partial \theta}\frac{\partial \theta}{\partial \Lambda} \tag{9.20}$$

$$\frac{\partial F_{WI}}{\partial C_{L_\perp}} = \frac{F_{WI}}{C_{L_\perp}} \tag{9.21}$$

9.3.1.2 $F_{W_{vol}}(M_\infty, \Lambda, C_{L_\perp})$

$$F_{W_{vol}} = \frac{4\tau^2}{M_\infty C_{L_\perp}\sigma^2}(\tan^2\Lambda + \sigma^2)\Re\{Z_2\} \tag{9.22}$$

$$\Re\{Z_2\} = \frac{1}{r^{\frac{3}{2}}}\left\{\phi\cos\frac{3\theta}{2} - 3\psi\sin\frac{3\theta}{2}\right\} \tag{9.23}$$

$$\frac{\partial(\Re\{Z_2\})}{\partial r} = \frac{-3}{2r}\Re\{Z_2\} \tag{9.24}$$

$$\frac{\partial(\Re\{Z_2\})}{\partial\theta} = \frac{-3}{2r^{\frac{3}{2}}}\left\{\phi\sin\frac{3\theta}{2} + 3\psi\cos\frac{3\theta}{2}\right\} \tag{9.25}$$

$$\frac{\partial\Re\{Z_2\}}{\partial\phi} = \frac{1}{r^{\frac{3}{2}}}\cos\frac{3\theta}{2} \tag{9.26}$$

$$\frac{\partial\Re\{Z_2\}}{\partial\psi} = \frac{-3}{r^{\frac{3}{2}}}\sin\frac{3\theta}{2} \tag{9.27}$$

$$\frac{\partial F_{W\,vol}}{\partial M_\infty} = F_{W\,vol}\left[\frac{1}{\Re\{Z_2\}}\frac{\partial(\Re\{Z_2\})}{\partial M_\infty} - \frac{1}{M_\infty}\right] \tag{9.28}$$

$$\frac{\partial(\Re\{Z_2\})}{\partial M_\infty} = \frac{\partial(\Re\{Z_2\})}{\partial r}\frac{\partial r}{\partial M_\infty} + \frac{\partial(\Re\{Z_2\})}{\partial\theta}\frac{\partial\theta}{\partial M_\infty} + \frac{\partial\Re\{Z_2\}}{\partial\phi}\frac{\partial\phi}{\partial M_\infty} \tag{9.29}$$

$$\frac{\partial F_{W\,vol}}{\partial\Lambda} = F_{W\,vol}\left[\frac{1}{\Re\{Z_2\}}\frac{\partial(\Re\{Z_2\})}{\partial\Lambda} + \frac{2\tan\Lambda(1+\tan^2\Lambda)}{\tan^2\Lambda+\sigma^2}\right] \tag{9.30}$$

$$\frac{\partial(\Re\{Z_2\})}{\partial\Lambda} = \frac{\partial(\Re\{Z_2\})}{\partial r}\frac{\partial r}{\partial\Lambda} + \frac{\partial(\Re\{Z_2\})}{\partial\theta}\frac{\partial\theta}{\partial\Lambda} + \frac{\partial\Re\{Z_2\}}{\partial\phi}\frac{\partial\phi}{\partial\Lambda} + \frac{\partial\Re\{Z_2\}}{\partial\psi}\frac{\partial\psi}{\partial\Lambda} \tag{9.31}$$

$$\frac{\partial F_{W\,vol}}{\partial C_{L_\perp}} = -\frac{F_{W\,vol}}{C_{L_\perp}} \tag{9.32}$$

9.3.1.3 $F_F(M_\infty, \Lambda, C_{L_\perp}, C_{D_{F_\perp}})$

$$F_F = \frac{C_{D_{F_\perp}}}{M_\infty C_{L_\perp}\cos^2\Lambda} \tag{9.33}$$

$$\frac{\partial F_F}{\partial M_\infty} = -\frac{F_F}{M_\infty} \tag{9.34}$$

$$\frac{\partial F_F}{\partial\Lambda} = 2F_F\tan\Lambda \tag{9.35}$$

$$\frac{\partial F_F}{\partial C_{L_\perp}} = -\frac{F_F}{C_{L_\perp}} \tag{9.36}$$

$$\frac{\partial F_F}{\partial C_{D_{F_\perp}}} = \frac{F_F}{C_{D_{F_\perp}}} \tag{9.37}$$

9.3.1.4 $F_P(M_\infty, \Lambda, C_{L_\perp}, C_{D_{P_\perp}})$

$$F_P = \frac{C_{D_{P_\perp}} \cos\Lambda}{M_\infty C_{L_\perp}} \tag{9.38}$$

$$\frac{\partial F_P}{\partial M_\infty} = -\frac{F_P}{M_\infty} \tag{9.39}$$

$$\frac{\partial F_P}{\partial \Lambda} = -F_P \tan\Lambda \tag{9.40}$$

$$\frac{\partial F_P}{\partial C_{L_\perp}} = -\frac{F_P}{C_{L_\perp}} \tag{9.41}$$

$$\frac{\partial F_P}{\partial C_{D_{P_\perp}}} = \frac{F_P}{C_{D_{P_\perp}}} \tag{9.42}$$

9.3.1.5 $F_{S_P}(M_\infty, \Lambda, C_{L_\perp}, C_{D_{P_\perp}})$

$$F_{S_P} = \frac{C_{D_{P_\perp}} \sin\Lambda}{M_\infty C_{L_\perp} \alpha_{S_P}} \tag{9.43}$$

$$\frac{\partial F_{S_P}}{\partial M_\infty} = -\frac{F_{S_P}}{M_\infty} \tag{9.44}$$

$$\frac{\partial F_{S_P}}{\partial \Lambda} = \frac{F_{S_P}}{\tan\Lambda} \tag{9.45}$$

$$\frac{\partial F_{S_P}}{\partial C_{L_\perp}} = -\frac{F_{S_P}}{C_{L_\perp}} \tag{9.46}$$

$$\frac{\partial F_{S_P}}{\partial C_{D_{P_\perp}}} = \frac{F_{S_P}}{C_{D_{P_\perp}}} \tag{9.47}$$

9.3.2 Elementary Variables

$$\beta^2 = {M_\infty}^2 - 1 \tag{9.48}$$

$$m' = \frac{(\sigma^2 - 1)\sin\Lambda\cos\Lambda}{\sin^2\Lambda + \sigma^2\cos^2\Lambda} \tag{9.49}$$

$$n = \frac{\sigma}{\sin^2\Lambda + \sigma^2\cos^2\Lambda} \tag{9.50}$$

$$\frac{\partial\beta}{\partial M_\infty} = \frac{M_\infty}{\beta} \tag{9.51}$$

$$\frac{\partial m'}{\partial\Lambda} = (\sigma^2 - 1)\left\{\frac{\cos^2\Lambda - \sin^2\Lambda}{\sin^2\Lambda + \sigma^2\cos^2\Lambda}\right\} + 2m'^2 \tag{9.52}$$

$$\frac{\partial n}{\partial\Lambda} = 2m'n \tag{9.53}$$

$$r = \sqrt{4m'^2n^2 + (\beta^2 + n^2 - m'^2)^2} \tag{9.54}$$

$$\theta = \arctan\left\{(-2m'n), (\beta^2 + n^2 - m'^2)\right\} \tag{9.55}$$

$$\frac{\partial r}{\partial\beta} = \frac{2\beta}{r}(\beta^2 + n^2 - m'^2) \tag{9.56}$$

$$\frac{\partial r}{\partial m'} = \frac{2m'}{r}(2n^2 - (\beta^2 + n^2 - m'^2)) \tag{9.57}$$

$$\frac{\partial r}{\partial n} = \frac{2n}{r}(2m'^2 + (\beta^2 + n^2 - m'^2)) \tag{9.58}$$

$$\frac{\partial\theta}{\partial\beta} = \sin\theta\cos\theta\left[-\frac{2\beta}{(\beta^2 + n^2 - m'^2)}\right] \tag{9.59}$$

$$\frac{\partial\theta}{\partial m'} = \sin\theta\cos\theta\left[\frac{1}{m'} + \frac{2m'}{(\beta^2 + n^2 - m'^2)}\right] \tag{9.60}$$

$$\frac{\partial\theta}{\partial n} = \sin\theta\cos\theta\left[\frac{1}{n} - \frac{2n}{(\beta^2 + n^2 - m'^2)}\right] \tag{9.61}$$

$$\phi = (\beta^2 + 2n^2 - m'^2) \tag{9.62}$$

$$\psi = m'n \tag{9.63}$$

$$\frac{\partial \phi}{\partial \beta} = 2\beta \tag{9.64}$$

$$\frac{\partial \phi}{\partial m} = -2m' \tag{9.65}$$

$$\frac{\partial \phi}{\partial n} = 4n \tag{9.66}$$

$$\frac{\partial \psi}{\partial m} = n \tag{9.67}$$

$$\frac{\partial \psi}{\partial n} = m \tag{9.68}$$

$$\frac{\partial r}{\partial M_\infty} = \frac{\partial r}{\partial \beta}\frac{\partial \beta}{\partial M_\infty} \tag{9.69}$$

$$\frac{\partial \theta}{\partial M_\infty} = \frac{\partial \theta}{\partial \beta}\frac{\partial \beta}{\partial M_\infty} \tag{9.70}$$

$$\frac{\partial \phi}{\partial M_\infty} = \frac{\partial \phi}{\partial \beta}\frac{\partial \beta}{\partial M_\infty} \tag{9.71}$$

$$\frac{\partial r}{\partial \Lambda} = \frac{\partial r}{\partial m'}\frac{\partial m'}{\partial \Lambda} + \frac{\partial r}{\partial n}\frac{\partial n}{\partial \Lambda} \tag{9.72}$$

$$\frac{\partial \theta}{\partial \Lambda} = \frac{\partial \theta}{\partial m'}\frac{\partial m'}{\partial \Lambda} + \frac{\partial \theta}{\partial n}\frac{\partial n}{\partial \Lambda} \tag{9.73}$$

$$\frac{\partial \phi}{\partial \Lambda} = \frac{\partial \phi}{\partial m}\frac{\partial m'}{\partial \Lambda} + \frac{\partial \phi}{\partial n}\frac{\partial n}{\partial \Lambda} \tag{9.74}$$

$$\frac{\partial \psi}{\partial \Lambda} = \frac{\partial \psi}{\partial m}\frac{\partial m'}{\partial \Lambda} + \frac{\partial \psi}{\partial n}\frac{\partial n}{\partial \Lambda} \tag{9.75}$$

Chapter 10
Results

Four airfoil sections are documented in this chapter; the initial starting geometry, RAE282214[1], (not optimized), a designed reference airfoil, OAW1465FB[2], and two designed comparison airfoils, OAW1265FB[3] and OAW1475FB[4]. Six operating points were considered for each airfoil at each freestream Mach number. Various constraints were formulated in order to achieve workable airfoil design solutions. To compare the accumulated objective function of two different airfoils, the operating points for the two airfoils must map to the same positions on the transonic drag rise polars. For airfoils of similar section but of differing thickness, the position of the knee shifts to higher Mach numbers as the thickness of the airfoil is reduced. The transonic equivalence parameter, κ, was used to achieve mapping between airfoils OAW1465FB and OAW1265FB where

$$\kappa = \frac{1 - {M_{\infty_\perp}}^2}{[{M_{\infty_\perp}}^2 \tau]^{\frac{2}{3}}} \tag{10.1}$$

Operating at different values of $C_{L_\perp}$ will also shift the knee of the drag polar. Higher lift loadings will strengthen shocks and thus shift the knee to lower Mach numbers. To account for this, a reduced set of perpendicular Mach numbers for airfoil OAW1475FB was compared with those of OAW1465FB. The mapping was achieved by inspection. Ten freestream flight Mach numbers, $M_\infty = 1.1, 1.2, \ldots, 2.0$, were optimized over, giving ten sweep angles per $M_{\infty_\perp}$ operating point. Equation 8.2 defines the sweep, examples of which are shown in table 10.1 together with a summary of interesting results. All designed airfoils had constrained thicknesses at 20% and 65% chord as a basis for the cabin shape. The thickness was either 12% or 14% chord at these locations. The first two numbers appearing in the OAW airfoil names correspond to this thickness. $C_{L_\perp}$

[1] initial guess airfoil – detailed in section 10.1.

[2] reference airfoil detailed in section 10.1.

[3] predominantly just a change in thickness from OAW1465FB – detailed in section 10.2.

[4] predominantly just a change in $C_{L_\perp}$ from OAW1465FB – detailed in section 10.3.

values of 0.65 and 0.75 were considered and are reflected by the second pair of numbers.

10.1 Reference Solution Airfoil OAW1465FB

Reference [7] suggested a 7ft. thick wing of 50 ft. span. With this in mind constraints were set up to create the airfoil OAW1465FB. This reference airfoil was constrained to deliver a lift coefficient of $C_{L_\perp} = 0.65$ whilst maintaining 14% thickness at 20% and 65% chord. The initial starting geometry was obtained by scaling the RAE2822 airfoil such that the required thickness constraint @ 65% chord could be enforced from the beginning (see figure 10.1). This made an extremely thick airfoil (RAE282214) but aided convergence. As the optimization proceeded, the airfoil was allowed to thin around the forward region. The forward thickness constraint was imposed once the airfoil had thinned appropriately. Figure 10.2 shows the partially converged airfoil geometry solution accompanied by the six operating point pressure distribution graphs. The drag polar, created by these operating points is also given. The bottom left of figure 10.2 lists certain quantities, including the accumulated objective function (summed over the freestream Mach numbers), for both the non-linear converged solution (baseline) and the linearly extrapolated prediction (modified). The airfoil was only partially optimized for the given constraints. This decision was made to stop an unfavorable characteristic that was developing. Left to converge under the given constraints, the optimum airfoil favored the "lip shape" (in this case shown for the thinner airfoil) of figure 10.3. Generating more of the required lift through the central camber benefitted the lower Mach number operating points by unloading the forwardly positioned shocks. It was assumed, however, that this shape would not be ideal for a cabin and so the optimization procedure was terminated at the point where the mid-chord began to pinch in significantly. Hence a flat base (OAW1465**FB**) was maintained. As can be seen from figure 10.2, the optimized airfoil has adopted the flattish upper surface so typical of transonic airfoils. This significantly reduced the shocks observed in figure 10.1. Airfoil RAE282214 was not considered as a sensible candidate for an OAW design but comparison between figures 10.1 and 10.2 clearly shows the benefits of relaxing the curvature along the upper surface. The thickness described at 20% and 65% was larger than the

optimum would be for a fixed volume only case. The upper surface in naturally driven to have low curvature since the upper surface shocks are so penalizing. The result, therefore, is deformation mainly on the lower side as shown by figures 10.2, 10.4 and 10.6. In effect the lower surface has been faired around the thickness constraints but in such a manner as to distribute the lift most efficiently. Fortunately, the resulting pitching moment values (about the quarter-chord, parallel with the major axis) were low in magnitude (~ -0.06). The thickness constraints caused a certain amount of over-speeding along the under surface local to the 20% and 65% chord positions. The flat base recovered some of the under side positive pressure with the spin-off of reduced maximum thickness.[5] Airfoil OAW1465FB has an interesting camber line. Specifically, the aft camber allows a more even lift distribution along the chord. In fact, an unusual degree of aft loading was tolerated even with the aft separation it induced. The acceptance of such high values of D_P is discussed in the conclusions section of this report.

10.2 Comparison Solution Airfoil OAW1265FB

This airfoil was designed to compare the thickness effect. The reference airfoil was scaled in the thickness direction only to define the initial geometry. This created an airfoil of equivalent chord but of reduced camber and thickness by the ratio 12:14. During subsequent optimization steps, constraints maintained the new 12% thickness at 20% and 65% chord. Again the optimization procedure was halted before too much waisting occurred at mid-chord. Figure 10.4 shows the solution. The effect of the maximum thickness on the total drag had little to do with volume due to the small significance of $D_{W_{vol}}$ on D (figure 7.11). However, since the thickness constraints for airfoils OAW1465FB and OAW1265FB were specified at the same ξ location, the rate at which the local thickness had to grow from the leading edge to reach that specified at 20% chord was less for the thinner airfoil. This resulted in airfoil OAW1265FB having an forward upper surface $C'_{P_\perp}$ of lower magnitude than that of OAW1465FB and thus the shocks were less severe. The same value of $C_{L_\perp}$ was specified so greater aft loading had

[5] the benefit this provides with respect to reduced $D_{W_{vol}}$ is very small.

to occur to make up for the initially lower $C'_{P_\perp}$. This made the value of $C'_{M\perp}$ worse. The result was a significant reduction in $C_{D_\perp}$ and $\mathcal{F}$ (compared with OAW1465FB) at the expense of cabin height (or extended chord length) and magnitude of pitching moment. The extra aft loading caused perpendicular pitching moments ~ -0.08.

10.3 Comparison Solution Airfoil OAW1475FB

Airfoil OAW1465FB was used as the initial starting airfoil to generate OAW1475FB. To make a fair comparison with airfoil OAW1465FB, an extra constraint had to be made. The thickness of OAW1465FB @ 40% chord was measured and imposed upon airfoil OAW1475FB. The range parameter benefitted immediately as can be seen by the sudden jump in the F_O history plot of figure 10.5. Further optimization allowed the new airfoil to generate the higher $C_{L_\perp}$ value with the help of mode deformation rather than just incidence. Achieving a higher value of $C_{L_\perp}$ through incidence alone tended to load up the airfoil heavily around the nose – thus penalizing the operating points associated with shocks in this region. Fixing the three thicknesses, but otherwise leaving the modes free, allowed more efficient generation of lift to be achieved whilst still maintaining the flat base. The solution airfoil is plotted in figure 10.6. The change in camber was achieved by a slight increase in maximum thickness through mainly upper surface deformation. This was very gradual to maintain small curvature on the upper surface and did not shift the loading significantly. The majority of extra lift was therefore achieved through increased incidence (about 1° which, characteristically, shifted the loading forward. This had the added bonus of reducing $C'_{M\perp}$ (now ~ -0.04). The greater load demand of $C_{L_\perp}$ caused the upper surface to have a higher $C'_{P_\perp}$ magnitude in general and also to shock sooner – hence the increased value of $C_{D_\perp}$. The extra lift generated outweighed the increase in drag, the result being a reduction in the objective function, F_O. This was all achieved at lower values of $M_{\infty_\perp}$, implying greater sweep values for the same freestream flight Mach numbers.

Table 10.1: Airfoil Characteristic Summary

Comparison of Interesting Quantities								
foil	$C_{L_\perp}$	τ_{max} @ 20% & 65%	$M_{\infty_\perp}$ oper. point	$M_{\infty_\perp}$	$\sum_{M_\infty=1.1}^{2.0} \mathcal{F}(M_\infty)$	$\alpha'_\perp$ (deg.)	$C'_{M\perp}$	Λ(deg.) @ $M_\infty = 1.6$
OAW 1465 FB	0.65	14%	1	.650	.493	4.7	-0.0645	66.0
			2	.700	.476	4.4	-0.0618	64.1
			3	.720	.477	4.3	-0.0606	63.3
			4	.730	.476	4.2	-0.0638	62.8
			5	.735	.479	4.2	-0.0643	62.6
			6	.740	.486	4.3	-0.0627	62.4
OAW 1265 FB	0.65	12%	1	.674	.476	4.0	-0.0794	65.1
			2	.722	.468	3.8	-0.0796	63.2
			3	.741	.470	3.5	-0.0859	62.4
			4	.750	.476	3.4	-0.0874	62.0
			5	.755	.477	3.5	-0.0882	61.8
			6	.760	.482	3.3	-0.0970	61.6
OAW 1475 FB	0.75	14%	1	.640	.470	5.7	-0.0427	66.4
			2	.680	.459	5.4	-0.0404	64.8
			3	.700	.455	5.1	-0.0446	64.1
			4	.710	.453	4.9	-0.0478	63.7
			5	.715	.457	4.9	-0.0486	63.5
			6	.720	.465	5.0	-0.0461	63.3

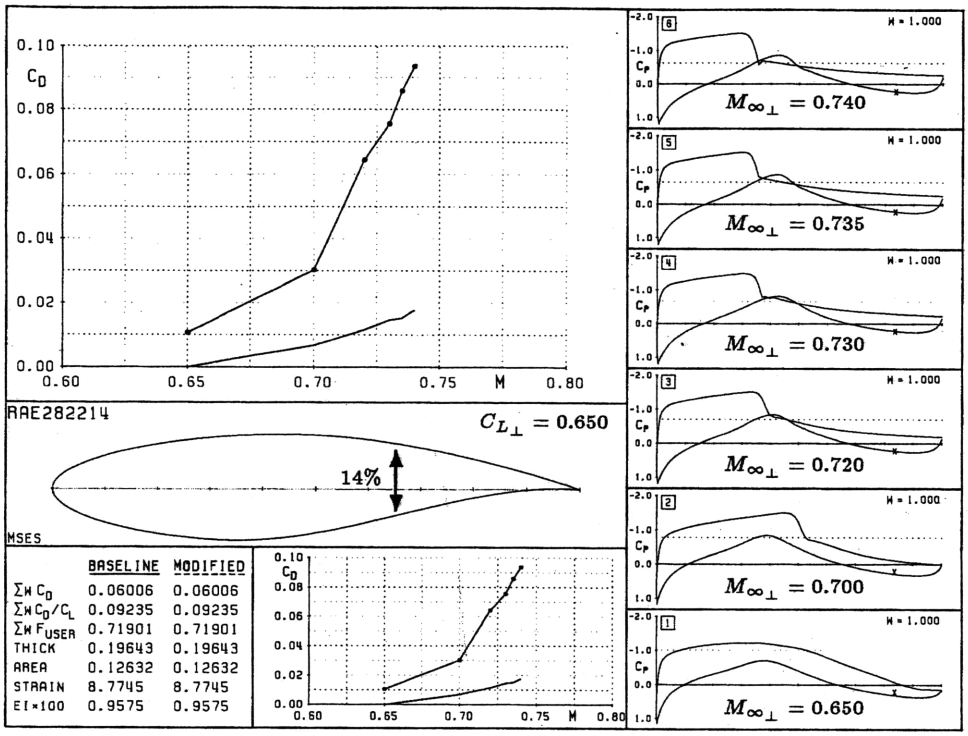

Figure 10.1: RAE282214 Airfoil Characteristics at $C_{L_\perp} = 0.65$

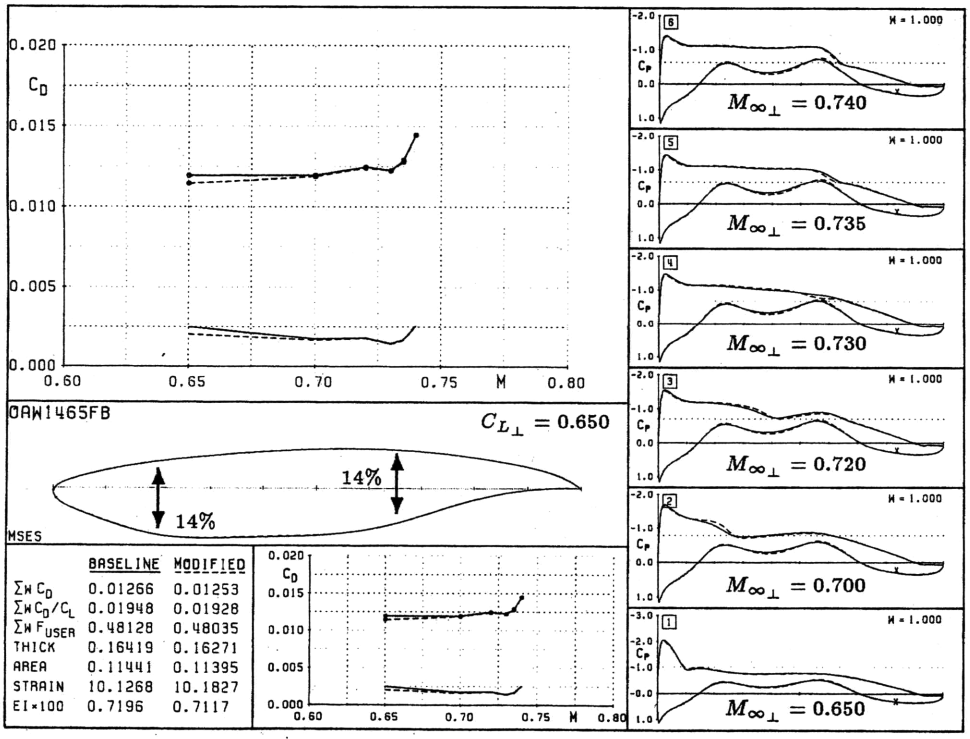

Figure 10.2: OAW1465FB Airfoil Characteristics at $C_{L_\perp} = 0.65$

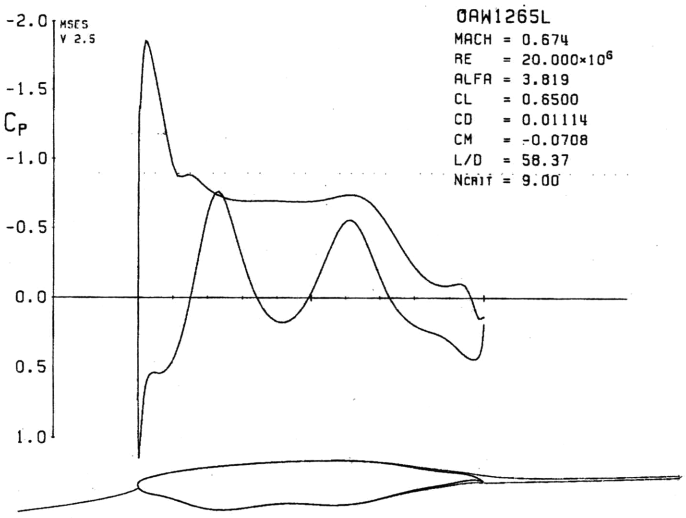

Figure 10.3: Lip shaped "over-optimized" airfoil

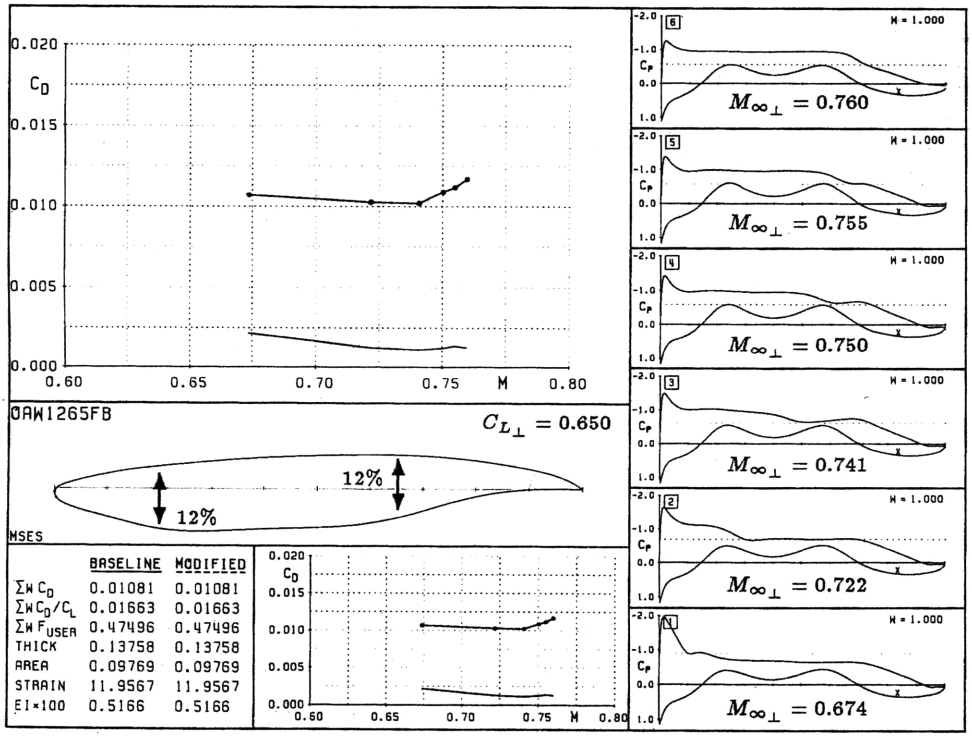

Figure 10.4: OAW1265FB Airfoil Characteristics at $C_{L_\perp} = 0.65$

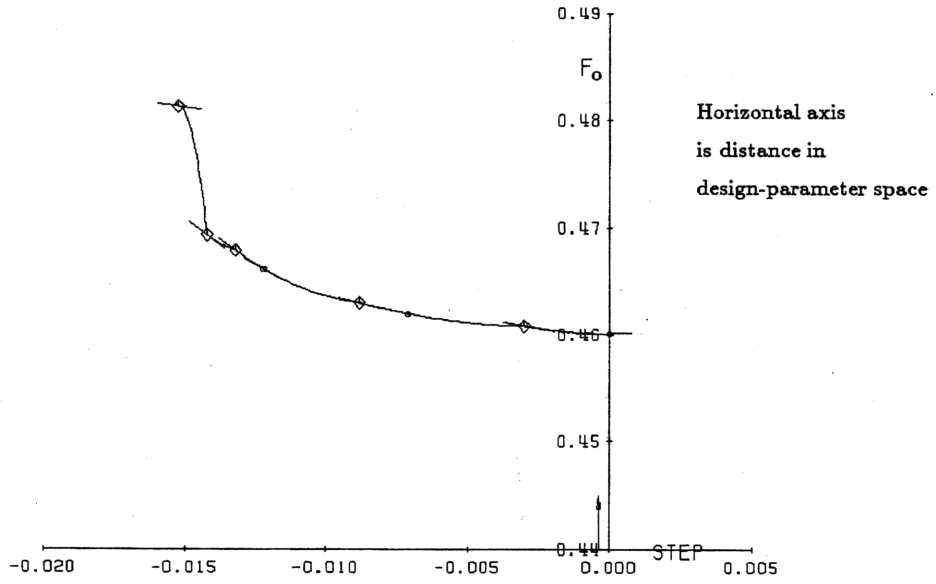

Figure 10.5: F_O Convergence History (OAW1465FB → OAW1475FB)

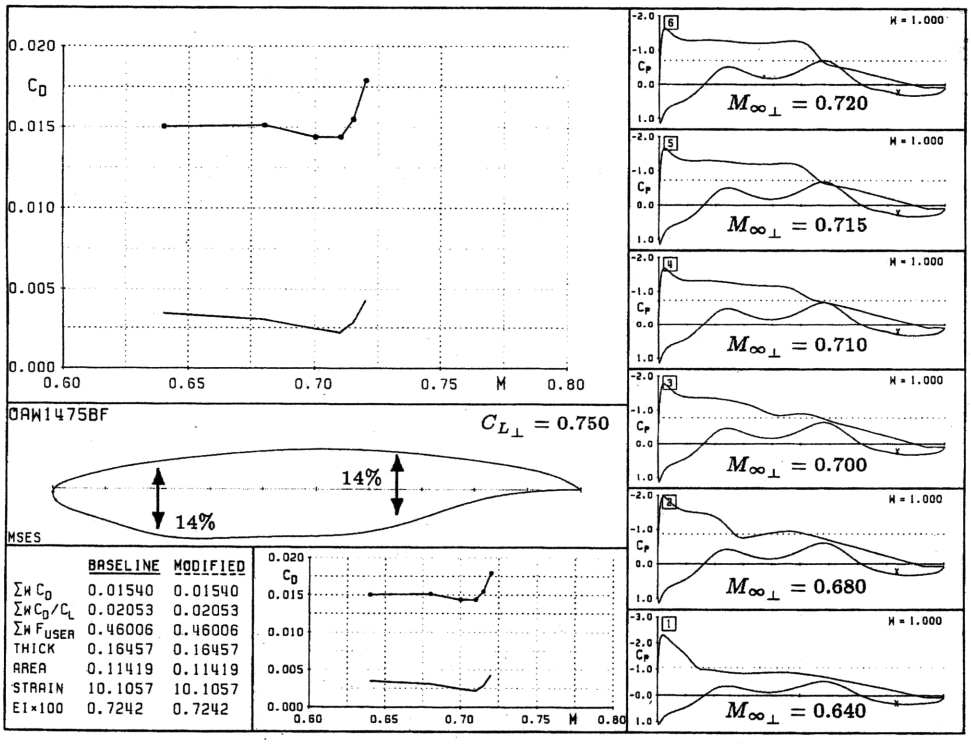

Figure 10.6: OAW1475FB Airfoil Characteristics at $C_{L_\perp} = 0.75$

Chapter 11
Conclusions

A few difficulties were encountered in the initial stages of design. In order to achieve a cabin style airfoil, a fair degree of user interaction was involved. The maximum thickness was constrained and the enclosed area set to create the required volume enclosure. The trailing edge angle was allowed to float in a controlled manner - visually avoiding geometric inflection induced by over constriction. Control over the pitching moment was used to encourage the desired cabin shape. Making use of LINDOP's inverse design option and steering the pressure distribution sped up the convergence. For example, the standing shock could be weakened and the under-side of the nose loaded up to reduce the lift local to the trailing edge. This process of user inspection/correction became more effective with experience. Specifying 24 mode shapes sometimes gave a little too much freedom to the high frequencies of deformation. This problem was avoided by initially setting fewer, lower frequency, DOF's until convergence was further down the line (similar idea to multi-grid techniques but for stability purposes rather than convergence speed). In all cases, ultimately seventeen mode-shapes were allowed – eight tied to the upper surface, eight to the lower and one localized at the nose. Since most deformation occurred on the under side, the weightings for the bottom surface modes were amplified to speed convergence. The early airfoil solutions were far from unique as so many variables were being constantly tweaked. A more successful approach (in terms of exemplifying the procedure) was adopted. User-defined restrictions were kept to a minimum and the dexterity of LINDOP increased[1] to allow multiple airfoil thickness constraints at defined locations. This removed the necessity to specify the enclosed area and pitching moment which were previously being used only to control geometry. During the design procedure a certain amount of "cosmetic touch-up" was carried out on the airfoil geometries using XFOIL[32]. As the airfoil deformed, certain regions became

[1] thanks Mark.

fairly insensitive to change. For instance, the under surface of the nose became very flat during the process of achieving desired local loading. The position of the stagnation point was then fairly free and hence the geometry pretty unconstrained. A small degree of volume could be obtained by gently bulging the shape out in this region with little effect on either $C_{D_\perp}$ or F_O. Occasionally, the airfoil surface would become wavy due to the mode shape specifications. Ultimately this was not a problem, it merely perturbed the convergence history. However, convergence could be accelerated "by hand" with a little smoothing. An under-constrained problem arose during the designs and is shown in the results section. With just two thickness constraints, the airfoil was free to deform in a manner only to minimize F_O – the resulting airfoil is shown in figure 10.3. The optimization wanted to pinch the airfoil in around the center allowing more of the lift to be generated through this induced camber. The benefit here is an aft shift of the center of pressure – the more lift that can be generated after the shock, the less the shock strength for a fixed $C_{L_\perp}$. This was a good example of the user becoming aware of required constraints **during** the procedure as opposed to at the start.

It was interesting to see that relatively large amounts of trailing-edge separation could be tolerated without significantly penalizing the objective function. The separation manifests itself in perpendicular pressure drag. Thus at high sweep angles, its streamwise component D_P is relatively small. Acceptance of high values of $D_{P_\perp}$ at large sweep angles leads to an airfoil design that is more intent on reducing the perpendicular drag values at lower sweeps. ie., for the same operating points (same sweep angle and perpendicular Mach number) the points lying on the dashed line of figure 11.1 may be more desirable than those of the solid line even though the sum of the perpendicular drag coefficients is higher and the highest operating point further up the drag polar. This implies a need for careful consideration of the choice of operating points to sum over. With an unswept wing the classically optimized airfoil would have the drag polar characteristic shown by the solid line of figure 11.1. Including more points at lower Mach number would not change the ideal airfoil section (based upon perpendicular coefficients). The swept wing drag, however, has dependencies on Λ which are hidden when viewing perpendicular drag values alone. The significance of the individual operating points are implicitly weighted with respect to Λ (see chapter 9.1 for exact functional

dependencies). Therefore, enough operating points must be chosen to avoid strictly localized optimization but the distribution of these points should be fairly close to the aircraft's desired operating conditions (eg., cruise). The above observation suggests that the initial desire to fly close to the knee of the drag polar may not be necessary. A plot of the objective function may be a more appropriate guide than that of $C_{D_\perp}$ during the process of narrowing down the initial, somewhat overwhelming, list of variables.

Wave drag analysis was the main driving force for suggesting the OAW. Somewhat ironically, the analysis presented herein showed profile drag to be the more dominant driver of wing sweep. For the cylindrical wing, only the perpendicular airfoil section is responsible for the generation of lift. Therefore, to fly at the maximum $\frac{L}{D}$ for any given freestream Mach number and sweep angle it is required that $M_{\infty_\perp}$ and $C_{L_\perp}$ be optimal. Previous work suggests operating at the knee of the transonic drag-rise curve and so necessitates a greater sweep angle than dictated by wave and induced drag alone.[2] Hence the objective function minima lie further to the right than suggested by figure 7.3 which considers wave drag due to lift only.

Specifying the perpendicular lift coefficient, $C_{L_\perp}$, to be a constant effectively removes the weighting of induced[3] drag on the objective function because C_L now drops at the rate of $\cos^2\Lambda$ with increasing sweep. Although D_F is independent of sweep, as sweep is increased lift is lost and $\mathcal{F}$ diminishes. D_F is now the only influence against opting for higher sweep angles – see figure 7.11. This requires flight altitude to be reduced as sweep is increased, in order to maintain the same true lift.

The type and scale of constraints required are not realized until the optimization procedure is underway. With so many variables to chose from it becomes almost impossible to determine the optimum airfoil choice, due to the extent of user interaction inevitably required, without first exploring a subset of avenues. This became a purpose of this report – the two subsets being a controlled thickness scale and controlled $C_{L_\perp}$. But as well as the documented examples contained within this report a certain amount

[2] later it was found that higher values of $M_{\infty_\perp}$ could be tolerated which slightly reduces the necessary angle of sweep.

[3] Induced drag: Ambiguity can be removed by expressing "drag due to lift" more correctly as drag due to C_L.

of 'playing' was done in an attempt to ascertain trends of airfoil choice. For instance, a few cases were run where the value of $C_{L_\perp}$ was allowed to float. The benefits of increasing $C_{L_\perp}$ with respect to F_O seemed to over-power the pit-falls of increased drag. This suggested that the limit of $C_{L_\perp}$ was an issue of stability more than anything else up to the point when the drag explodes due to massive separation and strong shocks. Of course, this assumes that a higher value of $C_{L_\perp}$ is always desired. Other thicknesses were also considered. In specifying thick airfoils the problem of gross separation was sometimes encountered. To avoid this problem thicker airfoils must fly at reduced $M_{\infty_\perp}$ which can be achieved by increasing sweep for any given M_∞. Due to the desire for high speed, the sweep angle already has high demands. As was noted before, at $M_\infty = 1.6$, a sweep angle of around 65° is expected. Further demands on Λ are undesirable. Although it has been shown that a significant amount of separation can be accepted, no special consideration is made in the objective function of the substantial spanwise flow that is associated with separated flow over highly swept wings. Thus, the validity of this result deteriorates with increasing degrees of separation.

Stipulating hypothetical restrictions allowed general trends to be explored. Enlightening results could be achieved with prior information concerning required cabin volume, location of structural members, pitching moment stipulations etc. to give realistic constraints. During the design process, it became apparent that the airfoil design was dramatically dependent upon these constraints. The designer will be thus be working under heavy trade-offs between passenger housing/comfort and fuel economy.

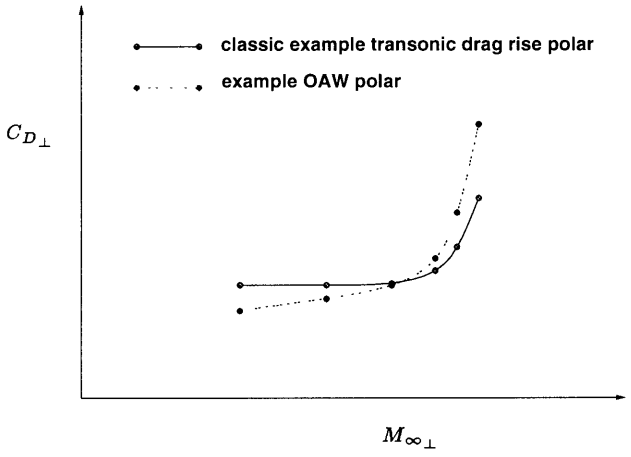

Figure 11.1: Perpendicular Transonic Drag Rise polars

Chapter 12

Future Improvements of the OAW Airfoil Design

No account was made for the drag of the engine nacelles. The nacelles will create profile drag and wave drag. The interference drag between the nacelles and the wing could also be evaluated. Normal practice would be to waist the fuselage around the nacelles – or the wing in this case. Ashley and Landahl[27] show a method for determining wave drag interference due to lift and volume. These drag contributors will be functions of sweep and freestream Mach number and thus may perturb the minimum of the new objective function. For simplicity an elliptic planform was considered in this report. Practicality may dictate other planforms such as a rectangular mid-section and tapered out-board sections. The objective function could be changed to model this planform. Should a wing and body combination be of interest, the current method would be appropriate except that the wave and profile drag of the fuselage (eg. Sears Haack) and the corresponding interference drag should also be calculated. Again, the wave drag component would be a function of Mach number and so the minimum may shift (presumably to favor elongation in the freestream direction). An important point to consider with the latter configuration would be the impingement of the fuselage shock upon the wing specifically concerning the possibility of shock induced separation. The direction of the streamlines over the wing played no quantitative role in this report. The extent of spanwise flow could be studied with intent to determine possible spanwise boundary layer thickening and control surface effectiveness – a 3D viscous/inviscid code coupled with the boundary layer would be enlightening. Should high lift devices be required, advantage could be taken of the multi-element capabilities of MSES.

Appendix A

Nomenclature

a'	Aerodynamic semi-chord at wing root See Fig.7.4 and Section 7.1.1
$\tilde{b}$	Geometric Span
b'	Aerodynamic semi-span See Fig.7.4 and Section 7.1.1
c	Geometric Chord
$\tilde{c}$	Geometric Root Chord
$C_{D_{F_\perp}}$	Perpendicular Friction Drag Coefficient
$C'_{D_{F_\perp}}$	Perpendicular Section Friction Drag Coefficient
$C_{D_{P_\perp}}$	Perpendicular Pressure Drag Coefficient
$C'_{D_{P_\perp}}$	Perpendicular Section Pressure Drag Coefficient
$C_{D_{WI}}$	Coefficient of Drag due to lift (inviscid)
$C_{D_{W_{vol}}}$	Coefficient of Wave Drag due to volume (inviscid)
C_L	Lift Coefficient ($C_L = \frac{L}{\frac{1}{2}\rho_\infty {V_\infty}_\perp{}^2 S}$)
$C_{L_\perp}$	Perpendicular Lift Coefficient
$C'_{L_\perp}$	Perpendicular Section Lift Coefficient
$C'_{P_\perp}$	Perpendicular Section Pressure Coefficient ($C'_{P_\perp} = \frac{p-p_\infty}{\frac{1}{2}\rho_\infty {V_\infty}_\perp{}^2}$)
$C'_{M\perp}$	Perpendicular Section Moment Coefficient about the Wing quarter-chord (geometric cho
D	True Total Drag $D = D_{WI} + D_{Wvol} + D_F + D_P + D_{S_P}$
$\mathcal{D}$	True Total Drag + Loss in Thrust due to Thrust Vectoring ($D + D_\epsilon$)
DE	Drag resulting from Engine Vectoring
D_{ll}	Lifting-line drag
D_{S_P}	Drag resulting from side-force reaction
D_F	Friction Drag on Aerofoil (2D)
D_P	Pressure Drag on Aerofoil (2D)
D_{WI}	Wave[1] and induced drag due to lift (3D inviscid)

$D_{W\,vol}$	Wave drag due to volume
$\mathcal{F}$	Minimizing Function ($\mathcal{F} = \frac{D}{M_\infty L} = \frac{1}{\mathcal{R}} = F_{WI} + F_{W\,vol} + F_F + F_P + F_{S_P}$)
F_O	Accumulated Objective Function
F_F	$\mathcal{F}$ component based on D_F
F_P	$\mathcal{F}$ component based on D_P
F_{S_P}	$\mathcal{F}$ component based on D_{S_P}
F_{WI}	$\mathcal{F}$ component based on D_{WI}
$F_{W\,vol}$	$\mathcal{F}$ component based on $D_{W\,vol}$
F_{vec}	$\mathcal{F}$ component based on D_ϵ
i	The complex number $\sqrt{-1}$
L	Total Lift $L = \frac{1}{2}\rho_\infty {V_\infty}^2 S C_L = \frac{1}{2}\rho_\infty {V_{\infty_\perp}}^2 S C_{L_\perp}$
L'	Total Lift per unit span
m	$m = \frac{Y}{y_\mu}$ See Fig.7.1
m'	See Fig.7.4 and Section 7.1.1
M_∞	Freestream Mach Number
$M_{\infty_\perp}$	Perpendicular Component of Freestream Mach Number
P_M	Pitching Moment about the quarter-chord (geometric chord)
n	See Fig.7.4 and Section 7.1.1
q_∞	Freestream dynamic pressure ($q_\infty = \frac{1}{2}\rho_\infty {V_\infty}^2$)
r	Magnitude of complex variable
$\mathcal{R}$	Range Parameter ($\mathcal{R} = \frac{M_\infty L}{D}$, $\mathcal{R}(T) = \frac{M_\infty L}{T}$)
$\Re\{Z\}$	Real part of Z
Re	Reynolds number
S	Wing Planform Area ($S = 2\int_0^{\frac{\tilde{b}}{2}} c(\eta)\, d\eta = \frac{\pi \tilde{b} \tilde{c}}{4} = \frac{\pi \tilde{b}^2}{4\sigma}$)
S_P	Side-Force (created by lateral component of D_P)
t_{max}	Airfoil Maximum Thickness
T	the total required thrust output from the engines ($T = -D$)
V_∞	Freestream Air Velocity
$V_{\infty_\perp}$	Perpendicular Component of Freestream Air Velocity
X	Streamwise Length of Wing See Fig.7.4 & Fig.7.1
x_{trip}	Turbulence Trip Location
Y	Aerodynamic span See Fig.7.4 & Fig.7.1

y_μ	See Fig.7.1
$\alpha_\perp$	Airfoil Incidence
β	$\beta = \sqrt{M_\infty^2 - 1}$
κ	Transonic Equivalence Parameter
Δs	Change in Entropy
Λ	Wing Major-axis Sweep Angle See Fig.7.1 (usually referred to in degrees)
μ	Mach angle See Fig.7.1 (usually referred to in degrees)
ϕ	$\phi = \beta^2 + 2n^2 - m'^2$
ψ	$\psi = m'n$
ρ_∞	Freestream Air Density
σ	Axis Ratio (geometric aspect ratio, $\sigma = \frac{\tilde{b}}{\tilde{c}}$)
τ	thickness/chord ratio ($\tau = \frac{t_{max}}{c}$)

Appendix B

Glossary of Acronyms

BA	British Airways
DOF	Degrees of Freedom
HSCT	High Speed Civil Transport
JAL	Japan Airlines
OAW	Oblique All Wing
SIA	Singapore Airlines
SSBJ	Supersonic Business Jet
SST	Supersonic Transport

Appendix C

Subroutine, 'luser.f'. (A LINDOP routine)

```
      SUBROUTINE USRFUN(NEL,NPAR,IPNT, FP,
     &                  PAR, FP_PAR,
     &                  MAT, FP_MAT,
     &                  CLT, FP_CLT,
     &                  CDF, FP_CDF,
     &                  CDP, FP_CDP,
     &                  CMT, FP_CMT,
     &                  ARB, FP_ARB,
     &                  EIB, FP_EIB,
     &                  SGB, FP_SGB )
      IMPLICIT REAL (M)
      DIMENSION PAR(NPAR), FP_PAR(NPAR),
     &          ARB(NEL) , FP_ARB(NEL),
     &          EIB(NEL) , FP_EIB(NEL),
     &          SGB(NEL) , FP_SGB(NEL)
C------------------------------------------------------------
C     Returns user-defined objective function for one point.
C     Also returns the funstion derivatives wrt input parameters.
C
C     Input:  NEL     number of elements
C             NPAR    number of user-defined parameters
C             IPNT    operating point index
C             PAR(.)  user-defined parameters
C             MAT     normal Mach number
C             CLT     normal CL
C             CDF     normal friction CD
C             CDP     normal pressure CD
C             CMT     normal CM
C             ARB(.)  element area
C             EIB(.)  element stiffness
C             SGB(.)  element stress per unit moment
C
C     Output: FP      objective function
C             FP_()   dFP/d()
C
C     This particular sample routine defines the objective
C     function to be the range parameter D/ML including sweep
C     corrections.  It assumes the first user parameter PAR(1)
C     is the freestream Mach, which together with the normal
C     Mach CLT implicitly defines the sweep angle.  Some of
C     the design parameters (CM, area, ...) do not enter into
C     this particular definition of the objective function,
C     so their corresponding derivatives are returned as zero.
C
```

```
C-------------------------------------------------------------
      PI = 4.0*ATAN(1.0)
C
      FP              =  0.0
      DO 5 IPAR=1, NPAR
        FP_PAR(IPAR) =  0.0
 5    CONTINUE
      FP_MAT          =  0.0
      FP_CLT          =  0.0
      FP_CDF          =  0.0
      FP_CDP          =  0.0
      FP_CMT          =  0.0
C
      DO 7 N=1, NEL
        FP_ARB(N)     =  0.0
        FP_EIB(N)     =  0.0
        FP_SGB(N)     =  0.0
 7    CONTINUE
C
C
      DO 10 IPAR=1, NPAR
C----   freestream Mach is PAR(IPAR)
C----   sweep from Freestream Mach
        COSL          =  MAT/PAR(IPAR)
        COSL_MAT      =  1.0/PAR(IPAR)
        COSL_PAR      = -COSL/PAR(IPAR)
        DLAM          =  ACOS(COSL) * 180.0/PI
        DLAM_COSL     = -(180.0/PI) / SQRT(1.0 - COSL**2)
        DLAM_MAT      =  DLAM_COSL*COSL_MAT
        DLAM_PAR      =  DLAM_COSL*COSL_PAR
c
c.......hard code axis ratio
        SIG           =  10.0
c.......hard code thickness/chord
        TAU           =  0.15
c.......hard code side-force/drag
        SF_D          =  20.0
cc
C----   set objective function for this point
        CALL OAW(SIG,TAU,SF_D,PAR(IPAR),DLAM,CLT,CDF,CDP,
     &           F, F_PAR, F_DLAM, F_CLT, F_CDF, F_CDP)
        FP            =  FP            + F
        FP_PAR(IPAR) =  FP_PAR(IPAR) + F_PAR
     &                                 + F_DLAM*DLAM_PAR
        FP_MAT        =  FP_MAT        + F_DLAM*DLAM_MAT
        FP_CLT        =  FP_CLT        + F_CLT
        FP_CDF        =  FP_CDF        + F_CDF
        FP_CDP        =  FP_CDP        + F_CDP
 10   CONTINUE
      RETURN
      END
```

Appendix D

Subroutine, 'OAW.f'. (A LINDOP routine called by luser.f)

```
      SUBROUTINE OAW(SIG,TAU,SF_D,MINF,LAMDA,CLT,CDFT,CDPT,
     &               F,F_MINF,F_LAMDA,F_CLT,F_CDFT,F_CDPT)
c
c.....This routine expects the angle LAMDA to be in degrees.
c.....The derivative F_LAMDA is output wrt degrees.
c
      IMPLICIT NONE
c.....input variables
      REAL SIG,TAU,SF_D,MINF,LAMDA,CLT,CDFT,CDPT
c.....output variables
      REAL F,F_MINF,F_LAMDA,F_CLT,F_CDFT,F_CDPT
c.....Local variables
      REAL PI,MU,RLAM
      REAL C,C2,S,S2,T,T2,B2
      REAL BETA,m,n,r,THETA
      REAL FWI,FWV,FF,FP,FS,RZ1,RZ2
      REAL PHI,PSI
c.....Local derivative variables
      REAL FF_CDFT
      REAL FP_CDPT,FS_CDPT
      REAL BETA_MINF,m_LAMDA,n_LAMDA
      REAL r_BETA, THETA_BETA, PHI_BETA
      REAL r_m,    THETA_m,    PHI_m,    PSI_m
      REAL r_n,    THETA_n,    PHI_n,    PSI_n
      REAL r_MINF, THETA_MINF, PHI_MINF
      REAL r_LAMDA,THETA_LAMDA,PHI_LAMDA,PSI_LAMDA
      REAL RZ1_r, RZ1_THETA
      REAL RZ2_r, RZ2_THETA, RZ2_PHI, RZ2_PSI
      REAL RZ1_MINF, RZ1_LAMDA
      REAL RZ2_MINF, RZ2_LAMDA
      REAL FWI_MINF,FWV_MINF,FF_MINF,FP_MINF,FS_MINF
      REAL FWI_LAMDA,FWV_LAMDA,FF_LAMDA,FP_LAMDA,FS_LAMDA
      REAL FWI_CLT,FWV_CLT,FF_CLT,FP_CLT,FS_CLT
c
c.....Define PI
      PI          =   4.0*ATAN(1.0)
c.....Determine Mach angle, MU (in degrees)
      MU          =   ASIN(1.0/MINF) *180.0/PI
c.....test to check that the wing is swept behind the mach angle...
```

```
      IF ( LAMDA.LT.(90.0-MU) ) THEN
         GOTO 99
      ENDIF
c.....RLAM is LAMDA in radians
      RLAM         =   LAMDA*PI/180.0
      C            =   COS(RLAM)
      C2           =   C**2
      S            =   SIN(RLAM)
      S2           =   S**2
      T            =   TAN(RLAM)
      T2           =   T**2
      B2           =   MINF**2-1
      BETA         =   SQRT(B2)
      m            =  (SIG**2-1.0)*S*C/(S2+(SIG*C)**2)
      n            =   SIG/(S2+(SIG*C)**2)
      THETA        =   ATAN2(-2.0*m*n,(B2+n**2-m**2))
      r            =   SQRT(4.0*(m*n)**2+(B2+n**2-m**2)**2)
      PHI          =   B2+2.0*n**2-m**2
      PSI          =   m*n
      RZ1          =   SQRT(r)*(COS(THETA/2.0))
      RZ2          =  (PHI *COS(1.5*THETA) -
     &                 3.0*PSI*SIN(1.5*THETA))/r**1.5
      FWI          =   CLT*C2*RZ1/(4.0*MINF)
      FWV          =   4.0*TAU**2*(T2+SIG**2)*RZ2/(MINF*CLT*SIG**2)
      FF           =   CDFT/(MINF*CLT*C2)
      FP           =   CDPT*C/(MINF*CLT)
      FS           =  (CDPT*S/(MINF*CLT))/SF_D
c
      F            =   FWI+FWV+FF+FP+FS
c
c.....primary derivatives...
      BETA_MINF    =   MINF/BETA
      m_LAMDA      =  (SIG**2-1.0)*((C2-S2)/(S2+SIG**2*C2)) + 2.0*m**2
      n_LAMDA      =   2.0*m*n
      r_BETA       =   2.0*BETA*(        B2+n**2-m**2)/r
      r_m          =   2.0*m*(2.0*n**2-(B2+n**2-m**2))/r
      r_n          =   2.0*n*(2.0*m**2+(B2+n**2-m**2))/r
      THETA_BETA   =   SIN(THETA)*COS(THETA)*(  -2.0*BETA/(B2+n**2-m**2))
      THETA_m      =   SIN(THETA)*COS(THETA)*(1.0/m+2.0*m/(B2+n**2-m**2))
      THETA_n      =   SIN(THETA)*COS(THETA)*(1.0/n-2.0*n/(B2+n**2-m**2))
      PHI_BETA     =   2.0*BETA
      PHI_m        =  -2.0*m
      PHI_n        =   4.0*n
      PSI_m        =   n
      PSI_n        =   m
c
      r_MINF       =   r_BETA    *BETA_MINF
      THETA_MINF   =   THETA_BETA*BETA_MINF
      PHI_MINF     =   PHI_BETA  *BETA_MINF
c
      r_LAMDA      =   r_m*    m_LAMDA+r_n*    n_LAMDA
      THETA_LAMDA  =   THETA_m*m_LAMDA+THETA_n*n_LAMDA
      PHI_LAMDA    =   PHI_m  *m_LAMDA+PHI_n  *n_LAMDA
      PSI_LAMDA    =   PSI_m  *m_LAMDA+PSI_n  *n_LAMDA
```

```
c
      RZ1_r       =   RZ1/(2.0*r)
      RZ1_THETA   =  -RZ1*TAN(THETA/2.0)/2.0
      RZ1_MINF    =   RZ1_r*r_MINF +RZ1_THETA*THETA_MINF
      RZ1_LAMDA   =   RZ1_r*r_LAMDA+RZ1_THETA*THETA_LAMDA
c
      RZ2_r       =  -1.5*RZ2/r
      RZ2_THETA   =  -1.5*(PHI*SIN(1.5*THETA) +
     &                3.0*PSI*COS(1.5*THETA))/r**1.5
      RZ2_PHI     =   COS(1.5*THETA)/r**1.5
      RZ2_PSI     =  -3.0*SIN(1.5*THETA)/r**1.5
c
      RZ2_MINF    =   RZ2_r*r_MINF+RZ2_THETA*THETA_MINF+
     &                RZ2_PHI*PHI_MINF
      RZ2_LAMDA   =   RZ2_r*r_LAMDA+RZ2_THETA*THETA_LAMDA+
     &                RZ2_PHI*PHI_LAMDA+RZ2_PSI*PSI_LAMDA
c
      FWI_MINF    =   FWI*(RZ1_MINF /RZ1-1.0/MINF)
      FWV_MINF    =   FWV*(RZ2_MINF /RZ2-1.0/MINF)
      FF_MINF     =  -FF/MINF
      FP_MINF     =  -FP/MINF
      FS_MINF     =  -FS/MINF
c
      FWI_LAMDA   =   FWI*(RZ1_LAMDA/RZ1-2.0*T   )
      FWV_LAMDA   =   FWV*(RZ2_LAMDA/RZ2+2.0*T*(1.0+T2)/(T2+SIG**2))
      FF_LAMDA    =   FF*2.0*T
      FP_LAMDA    =  -FP*T
      FS_LAMDA    =   FS/T
c
      FWI_CLT     =   FWI/CLT
      FWV_CLT     =  -FWV/CLT
      FF_CLT      =  -FF/CLT
      FP_CLT      =  -FP/CLT
      FS_CLT      =  -FS/CLT
c
      FF_CDFT     =   FF/CDFT
c
      FP_CDPT     =   FP/CDPT
      FS_CDPT     =   FS/CDPT
c
      F_MINF      =  FWI_MINF+FWV_MINF+FF_MINF+FP_MINF+FS_MINF
      F_LAMDA     =  FWI_LAMDA+FWV_LAMDA+FF_LAMDA+FP_LAMDA+FS_LAMDA
c.....output F_LAMDA with dimensions per degree...
      F_LAMDA     =  F_LAMDA * PI/180.0
      F_CLT       =  FWI_CLT+FWV_CLT+FF_CLT+FP_CLT+FS_CLT
      F_CDFT      =  FF_CDFT
      F_CDPT      =  FP_CDPT+FS_CDPT

      RETURN
c
 99   PRINT*,'error in routine OAW, wing is not swept behind mach line'
      RETURN
      END
```

Bibliography

[1] M. Drela. Design and optimization method for multi-element airfoils. AIAA Paper 93-0969, Feb 1993.

[2] R. T. Jones. The minimum drag of thin wings in frictionless flow. *Journal of the Aeronautical Sciences*, 18(2), Feb 1951.

[3] R. T. Jones. New design goals and a new shape for the SST. *Aeronautics & Astronautics*, Dec 1972.

[4] R. T. Jones and J. W. Nisbet. Transonic transport wings – oblique or swept? *Aeronautics & Astronautics*, Jan 1974.

[5] R. T. Jones. The oblique wing – aircraft design for transonic and low supersonic speeds. *Acta Astronautica*, 4, 1977.

[6] J. Ott. High-speed transport study focuses on lower mach range. *Aviation Week & Space Technology*, Feb 1988.

[7] B. W. Henderson. Nasa Ames resumes effort to develop supersonic, oblique wing aircraft. *Aviation Week & Space Technology*, Jan 1992.

[8] G. Warwick. Nasa proposes 'flying wing'. *Flight International*, Sep 1992.

[9] Donoghue. Editorial: The need for speed. *Air Transport World*, Nov 1988.

[10] Mach 2; taxpayers nil. *The Economist*, May 1990.

[11] Science and technology: The last of its kind? *The Economist*, Feb 1991.

[12] Washington. Market studies indicate demand for high-speed civil transport. *Aviation Week & Space Technology*, Nov 1988.

[13] The New Airplane Development Group. High-speed civil transport study. NASA Contractor Report NAS1-18377, Boeing Company, Seattle, WA, 1989.

[14] M. Pilling. Small market demand for 600-seaters. *Interavia Aerospace Review*, Sep 1991.

[15] B. Sweetman. High-speed agreement. *Interavia Aerospace Review*, Jan 1991.

[16] J. P. Woolsey. Second-generation SST gathers momentum. *Air Transport World*, Jan 1991.

[17] D.A. Brown. British airways planning more supersonic charters from U.S. *Aviation Week & Space Technology*, May 1985.

[18] H. Banks. Son of concorde. *Forbes*, Nov 1990.

[19] C. A. Shifrin. Britain and France begin Concorde follow-on study. *Aviation Week & Space Technology*, May 1990.

[20] B. Sweetman. Civil supersonics: a less distant thunder. *Interavia Aerospace Review*, Jul 1990.

[21] A. Baldo. Barrier breaker. *Financial World*, Apr 1989.

[22] J. R. Wilson. Supersonic businessman. *Interavia Aerospace Review*, Apr 1991.

[23] H. S. Bruner. SSBJ: A technological challenge. *ICAO Journal*, Aug 1991.

[24] H. Schlichting. *Boundary-Layer Theory.* McGraw-Hill, Inc, New York, 1968.

[25] M. Drela. Newton solution of coupled viscous/inviscid multielement airfoil flows. AIAA-90-1470, 1990.

[26] R. T. Jones. Theoretical determination of the minimum drag of airfoils at supersonic speeds. *Journal of the Aeronautical Sciences*, 19(12), Dec 1952.

[27] H. Ashley and M. Landahl. *Aerodynamics of Wings and Bodies.* Dover Publications, Inc., Mineola, N.Y., 1985.

[28] R. T. Jones. *Wing Theory.* Princeton University Press, Princeton, New Jersey, 1990.

[29] J. H. B. Smith. Lift/drag ratios of optimised slewed elliptic wings at supersonic speeds. *Aeronnautical Quarterly*, 12, Aug 1961.

[30] M. Drela and M. B. Giles. Viscous-inviscid analysis of transonic and low Reynolds number airfoils. *AIAA Journal*, 25(10):1347–1355, Oct 1987.

[31] M. B. Giles and M. Drela. Two-dimensional transonic aerodynamic design method. *AIAA Journal*, 25(9):1199–1206, Sep 1987.

[32] M. Drela. XFOIL: An analysis and design system for low Reynolds number airfoils. In T.J. Mueller, editor, *Low Reynolds Number Aerodynamics*. Springer-Verlag, Jun 1989. Lecture Notes in Engineering, No. 54.